INFLUENCES OF SOLUTE SEGREGATION ON GRAIN BOUNDARY MOTION

By

Hao Sun

A Thesis submitted to the Faculty of Graduate Studies of

The University of Manitoba

in partial fulfillment of the requirement of the degree of

MASER OF SCIENCE

Department of Mechanical Engineering

University of Manitoba

Winnipeg, Manitoba

ABSTRACT

Nanocrystalline materials are polycrystalline solids with grain size in the nanometer range (< 100nm), which have been found to exhibit superior properties such as high magnetic permeability and corrosion resistance, as well as a considerably increase of strength when compared with their coarse grain counterparts. All those improved properties are attributed to the high volume fraction of grain boundaries (GBs). However, the high density of GBs brings a large amount of excess enthalpy to the whole system, making the nanostructures unstable and suffer from severe thermal or mechanical grain growth. In order to maintain the advantageous properties of nanocrystalline materials, it is necessary to stabilize GB and inhibit grain growth. While alloying has been found to be an effective way of achieving stabilized nanocrystalline metal alloys experimentally, the direct quantification of solute effects on GB motion still poses great challenge for investigating thermal stability of general nanocrystalline materials.

In this research, impurity segregation and solute drag effects on GB motion were investigated by extending the interface random-walk method in direct molecular dynamics simulations. It was found that the GB motion was controlled by the solute diffusion perpendicular to the boundary plane. Based on the simulation results at different temperatures and impurity concentrations, the solute drag effects can be well modeled by the theory proposed by Cahn, Lücke and Stüwe (CLS model) more than fifty years ago. However, a correction to the original CLS model needs to be made in order to quantitatively predict the solute drag effects on a moving GB.

ACKNOWLEDEMENTS

First and foremost, I would like to show my deepest gratitude to my supervisor, Professor Chuang Deng, a respectable, responsible and resourceful scholar, who gives me the opportunity to pursue my graduate study. He has enriched my knowledge of material sciences and provided me with valuable guidance in every stage of the writing of this thesis. Without his enlightening instruction, impressive kindness and patience, I could not have completed my thesis. His keen and vigorous academic observation enlightens me not only in this thesis but also in my future study. The good advice, support from him has been invaluable on both an academic and a personal level, for which I am extremely grateful.

In addition, I would like to express my gratitude and appreciation to my committee members, Dr. Chuang Deng from the Department of Mechanical Engineering, and Dr. Olanrewaju Ojo from the Department of Mechanical Engineering, Dr. Michael Freund from the Department of Chemistry. Thank you for reviewing my thesis and attending my defence.

I would also like to thank all my teachers who have helped me to develop the fundamental and essential academic competence. My sincere appreciation also goes to the University of Manitoba, particularly in the award of a University of Manitoba Graduate Scholarship that provided the necessary financial support for this research. The library facilities and computer facilities of the University, as well as the Western Canada Research Grid provided me some financial, academic and technical support for my research, which is really helpful.

I shall extend my thanks to my girlfriend, Miss Beijia Ge for all her encouragement and care. Hope I would get married and have a wonderful family with you in the future.

Last but not least, all my knowledge is indebted to my parents who are fantastic educators and hopefully they should be contented with what I have done for them, at least for the time being. I couldn't have achieved my engineering education without their unconditional love and support.

TABLE OF CONTENTS

TABLE OF FIGURES

CHAPTER 1 MOTIVATION AND OUTLINE OF THE THESIS

1.1. Motivation

Grain boundary (GB) motion in crystalline metals and alloys has been the focus of studies on microstructural evolution such as grain growth and recrystallization for decades [1–11]. One goal of particular interest is to accurately predict or measure the GB mobility with the presence of impurities. The reason is that grain growth, which is usually undesired during heat treatment or mechanical deformation of crystalline materials, especially when the grain sizes are in the nanometer scale, can be effectively hindered through the segregation of particular alloying elements [12–16]. In recent years, both controlled experiments[14,17], analytical modeling[17,18], and atomistic simulations[13,15] have suggested alloying as an effective approach to stabilize GB networks through the segregation of selected alloying elements at GBs. In particular, a regular solution model originally proposed by Cahn, Lücke and Stüwe (referred as CLS model) [1,10,19] has been widely used to study the solute drag effects on migrating GBs; it is assumed in the CLS model that the GB mobility is controlled by dopant diffusion.

Since it is extremely difficult to study the motion of individual GBs through controlled experiments, various methods based on molecular dynamics (MD) have been developed to extract GB mobility [4,7,9,20,21] with the rapid development of high performance computation. Nevertheless, almost all past simulations were limited to pure systems. One main reason is that most MD methods require unrealistically high driving forces to enable atom transfer across the boundary so that the overall GB migration can be detected in typical MD time scale [4,7,20,21]. On the other hand, the rate of boundary migration in impure systems is mainly determined by the diffusional process of the

impurities[1,2,10,19,22,23], which is too slow to be studied by MD. In addition, the simulation cell must be large enough to form a steady-state impurity profile normal to the GB plane [23]. Therefore, a direct quantification of the GB mobility with the presence of dopants from either experiments or simulations, which is the key to validate the CLS model and predict microstructure evolution in realistic alloy systems, is still missing.

1.2. Objectives of the Thesis

In this thesis, MD simulations were used with the recently developed interface-random-walk (IRWalk) method [14,29,30], which is capable of extracting GB mobilities based on purely thermal fluctuations, to directly quantify the GB mobility with the presence of impurities. In particular, this research has three major objectives:

1. To examine impurity segregation and precipitation through direct MD simulations.
2. To validate the CLS model and fill the gap between MD simulations and analytical modeling by extending the IRWalk method to impure systems and directly quantifying the mobilities of impure GBs under experimental conditions.
3. To extract the activation energy for GB motion with high concentration of impurities and compare the simulation results with experiments.

1.3. Outline of the Thesis

The thesis is organized as follows. In chapter 2, the brief literature review about the physical background of GB, nanocrystalline materials, grain growth and GB stabilization through alloying is introduced. Specifically, some basic knowledge of GB structure, GB stabilization, and the theoretical solute drag model describing the relation between GB mobility and impurity concentration is presented.

In chapter 3, the theory of atomistic simulations relevant to this research is presented. It outlines the fundamental knowledge of molecular dynamics simulation and embedded atom method potential. In addition, typical methods based on molecular dynamics simulations to extract GB mobility are introduced. Moreover, the adaptation of IRWalk method is introduced, which is the key tool used in this study to extract the GB mobility.

In Chapter 4 the simulation model used in this research is introduced, including the geometry, the environmental configuration, and simulation procedure.

In chapter 5 a direct quantification of the influences of impurities on GB mobility is presented. The deep correlation between activation energy for GB motion and impurity concentration is validated and a correction to the existing model is also proposed to better predict the solute drag effects in a moving GB.

In chapter 6 the major conclusions and contributions of the thesis are summarized and plans for future work are outlined.

CHAPTER 2 LITERATURE REVIEW

2.1. Physical Background of Grain Boundary

2.1.1. Basic Thermodynamic Characteristics of Grain Boundary

Grain boundary (GB) is two-dimensional interfacial defect in polycrystalline materials. It is the interface that separates two grains with different orientation but the same crystal structure (Figure 2.1). During the solidification progress of polycrystalline material, some small crystals form at various positions with random orientation at first, then they begin to grow up and impinge each other. When the solidification progress finish, the crystal orientation varies at each grain, and the boundary between adjacent grains are composed of atoms deviated from their original crystal position. This is how GBs form and their formation progress can be found in Figure 2.2. Since GBs could be treated as general interfaces, the thermodynamic treatment and properties of GB are also similar to that of phase interface. The main difference between GB and phase interface is that for GB the two regions have the same thermodynamic properties. When the space is isotropic and no extra force or potential field like electric, magnetic or elastic field is added, the same phase exists on each side of GB.

Figure 2.1 SEM-EBSI micrographs for Al [24]

Figure 2.2 Schematic diagrams of the various stages in the solidification of a polycrystalline material; the square grids depict unit cells; the black line in (d) represent GB [24]

Since the atoms in GB are not located at their perfect crystalline sites, they are typically considered as non-equilibrium crystal defects. Not like vacancies or interstitials, whose energy could be compensated by the configuration entropy, the GB is very unlikely to be produced by thermal fluctuations [25]. Moreover, in order for the whole system to reach global minimum energy, the total surface area of GB should be zero. Therefore, some external restrictions should be existed to maintain an equilibrium surface, such as fixed volume or fixed energy, or some lines or spaces that the GB must pass [25].

When GB exits in equilibrium with its adjacent grains, it has the structure named "Grain Boundary Complexion" by Catwell *et al.* in their review [26]. Complexion, by their definition, is "an interfacial material or strata that is in thermodynamic equilibrium with its abutting phase(s)". GB in a system could undergo an abruptly change of properties at some critical values of thermodynamic parameters, which is analogous to the phase transition in bulk material when concentration of solutes or temperature varies [26]. Such kind of change could have a huge influence on the kinetic properties of GB, e.g., mobility, diffusivity, sliding resistance, but less influence on the static properties, such as energy, space volume. This phenomenon is viewed as "GB complexion transitions" by Catwell *et al.* [26]. Based on this definition, it is possible for us to get a "complexion change diagram" about GB under different temperature or different concentration of impurities. In this research, alloying is considered as the strategy to achieve GB stabilization and based on the later discussion, the variance of solute concentration in GB could influence the GB mobility greatly, but has relatively small effect on GB activation energy.

In order to explain the transition of GB complexion, a fundamental thermodynamic concept of GB should be introduced first: the GB energy per unit area γ. It represents the work required to create a surface between two grains in polycrystalline materials. Also, it is a continuous function of the thermodynamic parameters, e.g. temperature (*T)*, pressure (*P)*, and chemical potential (μ_i). Therefore, it is possible at some particular temperature and pressure two or more complexions could co-exist. An example of the first-order complexion transition is shown in Figure 2.3 [26]. This Figure shows that when temperature or pressure varies, the GB would undergo a complexion change between complexion α and β. The GB energy γ is independent of this transformation.

This figure has been moved out because of copyright issue.

Figure 2.3 A schematic illustration of GB excess free energy c in a pure material as a function of (a) pressure and (b) temperature for two "competing" complexions [26].

Another kind of complexion transition is the change of geometrical structure. This is shown in Figure 2.4. Since it is possible for two or more complexion with different atomic structures to co-exist in the same GB, the GB complexion transformation would cause the increase of curvature in GB, or "faceting transition" as mentioned in the paper by Catwell *et al.* [26]. Another result is "dissociation transition", which separates one original GB into two GBs and each has a single complexion.

This figure has been moved out because of copyright issue.

Figure 2.4 A schematic illustration of the coexistence of two GB complexions[26].

2.1.2. Geometric Structure of GB

One major challenge for the study of GB is its complex geometric structure. For a GB, eight parameters are needed to describe it without ambiguity. Specifically, there are three Euler angles to characterize the orientation difference between the two grains, three vector components of the translation vector that characterizes the relative displacement of the two crystalline with respect to each other, and two angle components describe the orientation normal to the GB plane with respect to one of those two grains. The GB properties such as mobility, energy could all be expressed theoretically as a function of those eight parameters. However, only five of those parameters, the three Euler angles and two angle components describing GB plane orientation, could be influenced externally. The translation vector is controlled by energetic reasons and could be determined under some certain temperature, pressure, chemical composition, so it is not viewed as an external independent parameter [27].

Based on the five external independent parameters, all GBs are divided into three categories (the structure of the first two kinds of GB are shown in Figure 2.5): twist GB with GB plane perpendicular to the rotation axis, tilt GB with GB plane parallel to rotation axis and mixed GB with interface which cannot fit into the other two relationships. It is straightforward to distinguish the tilt and twist GB based on geometrical differences. When the GB plane has equivalent Miller indices with respect to both grains, it is named symmetric tilt GB. All other types of GBs are asymmetrical GBs.

Figure 2.5 Schematic representations of a tilt boundary (a) and a twist boundary (b) between two idealized grains [28].

2.1.3. Atomic structure of grain boundary

As was mentioned before, the atoms in GB are deviated from their equilibrium positions, so a question arises: how are those atoms arranged in GB? There are many hypothesis in history but now it is undoubtedly confirmed by experiments that GB is a crystal like interface which can be distinguished in two categories: low-angle GB and high-angle GB [25,27].

When the misorientation angle, which is the rotation angle between adjacent grains, is small enough, the GB is composed of an array of edge dislocations with Burger vector ***b*** of the same sign and magnitude. One example of low angle GB is when the edge dislocations are aligned in the way shown in Figure 2.6.

This figure has been moved out because of copyright issue.

Figure 2.6 Demonstration of how a tilt boundary results from an alignment of edge dislocations [24,27]

When the misorientation angle exceeds 15^{o}, those individual dislocations in low angle GB would overlap each other and are no longer distinguishable. Thus, the dislocations lose their identity and the GB cannot be described by the same model. At first glance high angle GB seems to be constructed with random atomic structure (Figure 2.7), but the current understanding of the structure of high angle GB is that high angle GB is formed by repeated structure units. This definition comes from the theory that in a

perfect crystal lattice all the atoms have a defined equilibrium position to minimize their total energy, so any deviation from their original periodical positions would cause an increase in the total energy. Thus the atoms in polycrystalline material, including those in GB, would intend to keep in their original crystal positions. In fact, some atomic positions in GB could coincide with ideal crystal positions. The term coincidence site lattice (CSL) is used to describe the atom sites in GB which coincide with the crystal positions. Since both the adjacent grain has periodic geometric structure, it is reasonable to infer that the CSL must also be periodic. In order to determine CSL, the misorientation angle and rotation axis must be known first, then extend both grains to let them overlap each other, all the superposition of these two crystals are coincidence lattice sites. The symbol Σ is normally used to represent the reciprocal value of density of coincidence sites as (Figure 2.8 is the geometric model of the 36.87^{o} [100] tile bicrystal with CSL)

$$\Sigma = \frac{\text{number of coincidence sites in an elementary cell}}{\text{total number of all lattice sites in an elementary cell}} \qquad (2.1)$$

This figure has been moved out because of copyright issue.

Figure 2.7 High-angle and low-angle tile boundaries in a soap bubble model [29]

This figure has been moved out because of copyright issue.

Figure 2.8 Geometric model of the 36.87^{o} [100] tilt bicrystal with simple cubic lattice. The circles represent the positions of individual atoms, the empty circles denote the coincidence sites [27].

In order to form CSL in GB, the two adjacent grains should have specific misorientation angle between each other. Only a few types of basic structure units could exist and therefore only a limited number of GB is formed completely by CSL units. There are seven different convex polyhedra for high angle GB structure: tetrahedron,

regular octahedron, pentagonal bipyramid, tetragonal dodecahedron, capped trigonal prism, capped trigonal prism, capped Archimedian prism and icosahedron [25,27]. Some of those basic units are shown in Figure 2.9. For the majority of GBs, their structure is a combination of those basic units. Examples of those common GB are shown in Figure 2.10, in which single unit GBs (a) and (b) can combine together to form a two-unit GB [30]. By comparing Figure 2.9 with Figure 2.6, it is clear that despite the misorientation angle, the GB structure could be represented by a repeated kite-shaped structural unit. The only difference is that for high angle GB those kite-shaped units are connected with each other, while in the low angle GB each kite-shaped unit has equal distance [31].

This figure has been moved out because of copyright issue.

Figure 2.9 Minimum energy MgO structures of the (a) Σ 5 tilt, (b) Σ 5 twist, and (c) Σ 17 tilt GBs [30]

This figure has been moved out because of copyright issue.

Figure 2.10 Structure of three [100] symmetrical tilt GBs in a bcc bicrystal (a) {013}, (b) {024}, (c) {037}. Circles and triangles represent two parallel (100) planes [27]

Due to the combination of different basic units in two-unit GB, some atoms cannot occupy CLS sites, thus increasing the total GB energy compared to the single units GB. The GB which consists of only single type of units has sharp minima at the energy-orientation plot, which is called singular. As mentioned in Section 2.1.2, of all the eight parameters that determine a GB, five of them can be influenced externally and it is possible to keep all the other four parameters constant while systematically varying the misorientation angle. An example for energy-angle dependence relation in Al GB is presented in Figure 2.11.

This figure has been moved out because of copyright issue.

Figure 2.11 Energy for symmetric tilt boundaries in Al produced by rotating around [100] axis (left) and [110] axis (right) [32]

In this research, an asymmetric $\sum 5$ GB in three types of Al-based alloys was simulated by molecular dynamics simulations using LAMMPS[33] with embedded-atom method potentials including Al-Ni[34], Al-Pb[35], and Al-Ti[36]. Since the focus of this research is on the influences of impurity on GB mobility and energy, all the five parameters were kept constant while the impurity concentration changed.

2.2. Nanocrystalline Material

In recent years, nanocrystalline materials, which have average grain size between 10-100 nm, have drawn large attention because they exhibit several attractive and promising properties that are absent in their coarse-grained counterparts, such as high magnetic permeability, high electronic resistance and increase in diffusivity [37,38]. In particular, one of the most important characteristics in nanocrystalline metals is the increase in strength levels, which lead to improvements in hardness and wear resistance [38–40]. In this section, the increase in strength levels with the decrease of grain size, which is known as Hall-Petch relation, will be explained.

According to Teleman *et al*. [41], "the yield stress of a polycrystalline material are composed of two parts: the yield strength of a constrained crystalline material; and the strengthening effect of GB". Since each crystalline has its unique cleavage plane and primary shear plane, in polycrystalline material with a completely random orientation

between adjacent grains of GB, the plastic deformation cannot move across GB as easily as it does in grain when stress is added on this material. As a result, dislocations would pile up at one side of the GB. Each dislocation has its own stress field and tends to push other dislocations near it. This accumulation process increases the stress near GB and finally sets up an equilibrium distribution of dislocations. Although the force between different dislocations is cancelled, it has a resultant force on the GB, triggering off a source in the other grain or in the GB. Based on the above discussion, the yield stress σ_Y of a polycrystalline material would be [41]

$$\sigma_Y = \sigma_i + \frac{k_y}{\sqrt{d}} \tag{2.1}$$

σ_i is the friction stress which opposes dislocation motion, d is the grain diameter, k_y is the microscopic stress intensity factor and has the same dimension as the macroscopic stress intensity factor *K*. The yield stress σ_Y is also the stress needed for plastic deformation to occur. Eq. 2.1 is called Hall-Petch relation and some experimental data is shown below in Fig. 2.12. When the grain size is smaller than 10nm, the Hall–Petch breakdown, which shows that the yield stress would decrease as the grain size decrease, is due to the enhancement of GB diffusive processes [46].

This figure has been moved out because of copyright issue.

Figure 2.12 Hall–Petch plot for pure Ni and Ni-alloys from coarse-grained pure specimens, to fully amorphous Ni-based alloys [46].

2.3. Grain Growth

2.3.1. Grain Growth due to Thermal Effects

One signature of nanocrystalline material is the high volume fraction of GB area. For instance, in nanocrystalline materials with average grain size of approximate 5 nm, the GB area would occupy 50 vol.% [12]. It can be found from the orientation-energy dependence shown in Figure 2.10 that most high-angle GBs are unstable, which means that the nanostructured material with high volume fraction of high-angle GBs is thermodynamically unstable. The grain size in nanocrystal tends to expand to transform the nanocrystal into a normal polycrystal with coarser grain. One example of thermally driven grain growth is shown in Figure 2.13 of nanocrystalline Ni.

This figure has been moved out because of copyright issue.

Figure 2.13 Left: nanocrystalline Ni as-deposited; right: annealed for 30min at 673K [12]

In the annealing experiments with nanocrystalline Ni samples, Klement *et al*. [12] found two different mechanism of grain growth. An annealing treatment at 523K led to abnormal grain growth, resulting in a dual microstructure, which introduced larger grains in the original nanocrystalline grain system. In contrast, when the same experiment was done at 573K they found a totally different, more uniform grain growth behavior.

The reason of abnormal grain growth in nanocrystalline materials at relatively lower temperature is the existence of low angle GBs in grains composed of sub-grains. To form a first growth rate those sub-grains only need to rotate slightly toward each other. At a sufficiently high temperature, the fluctuation of atoms in nanocrystalline materials

makes it possible for the high angle GBs to move into some “lower energy” state. Which one could move is purely random for all high angle GBs. But the dual microstructure is still observed and will not disappear until the temperature is high enough for all GBs to move. Therefore, there are three stages for grain growth: abnormal grain growth, normal grain growth, and grain growth toward equilibrium [12].

2.3.2. Grain Growth due to Mechanical Effects

Stress-assisted grain growth is common in nanocrystalline material when shear stress is added on it. Although there is no force normal to the GB plane, the shear force causes a relative translation of the grains parallel to the GB plane, which could couple to normal GB motion. This phenomenon is called shear-coupling effect and the normal GB motion triggered by it would cause grain growth. The theory of coupling GB motion would be discussed in section 2.5.1 [31].

One example of the mechanically driven growth is observed by Rupert and Schuh [42]. During the sliding wear process of the nanocrystalline Ni-W alloy, they found an obvious grain growth for grains with diameter 3nm (Figure 2.14 (e) and (f)). The surface is marked by a dashed white line and the sliding direction is into the page. From the TEM images, a discrete region can be seen where the grain growth is evident. Beyond this region, which is about 100-300nm, there is no distinct change of grain size. For those with grain size of 25 nm, the wear process led to little microstructural evolution in the sample shown in Figure 2.14 (c) and (d). The driving force for this microstructural change is deformation-driven structural evolution. The high density of deformation occurred on the surface during sliding contact would cause GB migration and grain

rotation due to shear-coupling effect. The accumulation of plastic deformation could finally give rise to grain growth.

Figure 2.14 Top-down SEM views of lamellae cut from (a) an as-deposited specimen and (b) the center of a wear track. Cross-sectional bright field TEM micrographs of (c) as-deposited and (d) wear track lamellae from the alloy with an initial grain size 25 nm;(e) as-deposited and (f) wear track lamellae from the alloy with initial grain size 3 nm [42].

2.4. Grain Boundary Stabilization through Alloying

2.4.1. Thermodynamic Stabilization of Grain Boundary by Alloying

In the previous section the basic concepts of grain growth, especially our research priority, the grain growth due to thermal effects have been introduced. The driving force for this kind of grain growth is the reduction of excess Gibbs free energy brought by GB. Due to the instability of GB in nanocrystalline material, various approaches have been considered by researchers to stabilize GB. Out of those approaches, alloying is considered the most effective which has been demonstrated to be able to stabilized GB network at high temperatures. For example, nanocrystalline alloy has superior high temperature behavior compared with their pure metal counterparts [14,43]. While our research links this stabilization to the alloying effect on kinetic properties such as the decrease of mobility, it is also believed that the stability may also derive from a thermodynamic reduction in GB energy [13,15,18,25,27,40,44]. Usually the GB energy per unit area, E_{GB}, is larger than zero. However, there is a trend for this excess energy of GB to reduce to zero by alloying with certain types of elements. With reduced GB energy, the driving force for grain growth could also vanish.

The basis for GB stabilization in nanocrystalline alloy is the inhomogeneous distribution of solutes where the solutes preferentially occupy the GB sites. Their occupation could reduce not only the GB energy but also the elastic strain energy due to the atom size mismatch. As shown in Figure 2.15, the average grain size can be controlled by the solute concentration in the alloy. This phenomenon has practical benefits because it can be applied to tailor the grain size in nanocrystalline alloy by adding given concentration of solute in alloy [43].

This figure has been moved out because of copyright issue.

Figure 2.15 Experimental grain size–composition relationship in electrodeposited Ni-W and Ni-P [43]

Specifically, a macroscopic system which is large enough to have constant pressure, temperature and *N* components has been analyzed by Lejček [27]. According to Lejček [27], the increase of internal energy due to GB is

$$dU = TdS - PdV + \sum_{i=1}^{N} \mu_i dn_i + E_{\mathrm{GB}} dA \tag{2.2}$$

S is the entropy of the system, V is the volume and n_i is the amount of component *i* and *A* is the GB area. The integration of this equation results in

$$U = TS - PV + \sum_{i=1}^{N} \mu_i n_i + E_{\mathrm{GB}} A \tag{2.3}$$

Compared with Eq. 2.2,

$$AdE_{\mathrm{GB}} = -SdT + VdP - \sum_{i=1}^{N} n_i d\mu_i \tag{2.4}$$

The Gibbs-Duhem equation requires

$$-SdT + VdP - \sum_{i=1}^{N} n_i d\mu_i = 0 \tag{2.5}$$

This equation is valid for homogeneous phase, so for both grains adjacent to GB it is satisfied. Compared with Eq. 2.5 and Eq. 2.4, the excess energy brought by E_{GB} could only be contributed by the energy of atoms in GB as follows

$$-S^{\mathrm{GB}}dT + V^{\mathrm{GB}}dP - \sum_{i=1}^{N} \Gamma_i d\mu_i = dE_{\mathrm{GB}} \tag{2.6}$$

Γ_i is the coverage of component *i* on the GB area, which is N_i^{GB}/A. When temperature and pressure is constant, in a binary system the well-known Gibbs free energy could be got [18]

$$dE_{\mathrm{GB}} = -\Gamma_{\beta} d(\mu_{\beta} - \mu_{\alpha}) = E_{\mathrm{GB}}^{0} - \Gamma_{\beta}\left(RT\ln\frac{N_{\beta}^{\mathrm{GB}}}{N^{\mathrm{GB}}} + \Delta H^{\mathrm{seg}}\right) \tag{2.7}$$

E_{GB}^{0} is the GB energy of pure crystalline material. The segregation enthalpy ΔH^{seg} could be interpreted as the difference of energy between a solute atom in the crystalline and in GB. N_{β}^{GB} is the number of atoms in GB area. X_{β}^{G} is the global solute concentration. It is evident that the GB energy could be reduced by the addition of solutes in GB area. The concentration of solutes in equilibrium could be obtained by the minimum of total Gibbs free energy of a binary polycrystalline alloy. This energy has the following expression (solvent α and solute β) [44]:

$$G = N_\alpha \mu_\alpha^0 + N_\beta \mu_\beta^0 + E_{\mathrm{GB}} A + N_\beta^{\mathrm{M}} \Delta H_{\beta \text{in M}}^{\mathrm{sol}} + N_\beta^{\mathrm{GB}} \Delta H_{\beta \text{in GB}}^{\mathrm{sol}}$$
$$+RT\left[N_\beta^{\mathrm{M}} \ln\left(\frac{N_\beta^{\mathrm{M}}}{N^{\mathrm{M}}}\right) + N_\alpha^{\mathrm{M}} \ln\left(\frac{N_\alpha^{\mathrm{M}}}{N^{\mathrm{M}}}\right)\right] + RT\left[N_\beta^{\mathrm{GB}} \ln\left(\frac{N_\beta^{\mathrm{GB}}}{N^{\mathrm{GB}}}\right) + N_\alpha^{\mathrm{GB}} \ln\left(\frac{N_\alpha^{\mathrm{GB}}}{N^{\mathrm{GB}}}\right)\right] \quad (2.8)$$

N_α and N_β are the total number of α and β atoms, μ_α^0 and μ_β^0 are the potentials of the respective materials. $\Delta H_{\beta \text{in M}}^{\mathrm{sol}}$ and $\Delta H_{\beta \text{in GB}}^{\mathrm{sol}}$ are the enthalpies of solution for a solute atom in the matrix and GB respectively. N_β^{GB} and N_β^{M} are the number of solute atoms in matrix and GB phase respectively. In equilibrium, the system as a whole should have minimum energy, and the variance of Gibbs free energy, δG, is equal to zero. Eq. 2.3 can be divided into two parts: the GB part, which is represented by the chemical potential and the grain part, which is a constant through our analysis

$$G = G_{\mathrm{M}} + \sum_{i=1}^{M} N_i^{\mathrm{GB}} \left(\mu_i^{\mathrm{GB}} - \mu_i^{M}\right) \quad (2.9)$$

From the equilibrium requirement $\delta G = 0$, $\partial G / \partial N_i^{\mathrm{GB}} = 0$, and

$$\Delta G = \sum_{i=1}^{M} \left(\mu_i^{\mathrm{GB}} - \mu_i^{M}\right) = 0 \quad (2.10)$$

The chemical potential in binary alloy system is

$$\mu_i^{\mathrm{GB}} = \mu_i^{0,\mathrm{GB}} + RT \ln\left(\gamma_i X_i^{\mathrm{GB}}\right), \mu_i^{\mathrm{M}} = \mu_i^{0,\mathrm{M}} + RT \ln\left(\gamma_i X_i^{\mathrm{M}}\right) \quad (2.11)$$

$X_i^{\mathrm{GB}} = N_i^{\mathrm{GB}} / N^{\mathrm{GB}}$ is the atom fraction of component i, γ_i is the activity coefficient of component i. $\mu_\beta^{0,\mathrm{GB}}$ and $\mu_\beta^{0,\mathrm{M}}$ is the standard chemical potential of component i in pure state at GB and grain. Combining Eq. 2.10 and Eq. 2.11, the segregation equation for solute β in binary system is

$$\frac{X_{\beta}^{\mathrm{GB}}}{1-X_{\beta}^{\mathrm{GB}}}=\frac{X_{\beta}^{\mathrm{M}}}{1-X_{\beta}^{\mathrm{M}}}\exp\left(\frac{\Delta H^{\mathrm{seg}}}{RT}\right),\Delta H^{\mathrm{seg}}=\mu_{\beta}^{0,\mathrm{GB}}-\mu_{\beta}^{0,\mathrm{M}}=\ \Delta H_{\beta\text{in GB}}^{\mathrm{sol}}-\Delta H_{\beta\text{in M}}^{\mathrm{sol}} \quad (2.12)$$

This equation is often used as

$$X_{\beta}^{\mathrm{GB}}=X_{\beta}^{\mathrm{M}}\exp\left(\frac{\Delta H^{\mathrm{seg}}}{RT}\right) \quad (2.13)$$

In our following discussion, X_{β}^{M} and X_{β}^{GB} are replaced by C_{∞} and C_{o} respectively. This equation explains the segregation behavior of solutes in GB and the inhomogeneity in GB area which has sites for solutes in a lower Gibbs energy [27]. Thermodynamically, as long as enough solutes atoms are segregated in GB, a stable nanocrystalline structure could exist. Also, another impact would hinder grain growth progress is the banishment of dopants from the GB to the lattice because of the decreased segregation sites caused by grain growth [13].

2.4.2. Detailed Behavior of Solutes in Grain Boundary

Despite its significance, there has been immense challenge when studying solutes behavior in GB experimentally because of the vast five parameter space of GB structure [45]. Moreover, three more atomistic parameters are needed to describe the atomic relaxation in GB [46]. Since Gibbs free energy is sensitive to atomistic changes, an experimental tool that is precise enough to capture tiny variances around GB is necessary. Usually GB segregation is studied by Auger electron spectroscopy, secondary ion mass spectroscopy, analytical electron microscopy, field ion microscopy, or atom probe tomography [27], but they could only provide an average values for the large number of

GBs they investigated. So the atomistic simulation is most common and precise tool in this area, which could focus on particular one type of GB and the influence of one atom.

From the research by Tang *et al.* [47] and Schuh *et al*. [43], the segregation behavior is also influenced by the solute concentration. In Tang's work, the segregation behavior is not clear until there is enough concentration in the nanocrystal. This trend is shown in Figure 2.16. Based on what Schuh has done through Monte Carlo simulation [43] , as the solutes concentration increase, the GB would become saturate and not be able to provide more sites for solute to segregate. So it is difficult to discern whether there is an obvious segregation behavior when the solute concentration is high (Figure 2.17(c)).

This figure has been moved out because of copyright issue.

Figure 2.16 Reconstructed atom probe images of the nanocrystalline Al. The large red spheres represent O atoms, the smaller blue spheres represent Ga atoms and the light green dots represent the Al matrix atoms [47]

This figure has been moved out because of copyright issue.

Figure 2.17 Visual representation of a single 3 nm grain from the Ni-W alloy, W atoms (red) are shown relatively larger than Ni atoms (blue) for clarity. (a) 1 at.% W and (b) 5% (c) 20% W [43]

In the research done by Millett *et al.* [44],two dimensional $\sum 7$ symmetric tilt GB in pure copper is used to determine how GB structure is influenced by adding one solute near the GB. They found that when the distance between the dopant and GB is beyond 7.0 Å, there is no distinct influence of the solute on E_{GB}. Other important factors are the atomic size mismatch and the solute concentration near GB. The larger the atomic size mismatch is, the more effective they could decrease E_{GB}, which means less solute

concentration is needed for the reduction of E_{GB} to zero. Although the $\sum 7$ symmetric tilt GB has special periodic structure at first, after the introduction of solutes, the total GB changed into a thin amorphous layer and loss their periodicity (Figures 2.18(a) and (b)).

This figure has been moved out because of copyright issue.

Figure 2.18 The GB structure of Cu with (a) two solvent atoms (colored red) and (b) 10 solvent atoms. The atomic size mismatch is 2.2 [44]

MD simulation was also used by Millett *et al.* [44] to investigate the movement of GB with a solute nearby. If there is a dopant near the GB, at first a curvature would be created to reduce E_{GB}. Then the whole GB would move up to the location of the solute, rather than pull down the solute (Figure 2.19).

This figure has been moved out because of copyright issue.

Figure 2.19 GB migration of Cu at 800 K [44]

2.5. Grain Boundary Motion and Solute Drag Effects

GB migration determines the granular microstructure during grain growth and recrystallization in metals [48], reflecting the physical, chemical and mechanical properties of this material. GB mobility describes the relation between velocity and driving force of GB migration. State-of-the-art engineering design of microstructures in material needs the GB mobility as an essential input parameter. In grain growth study, averaged GB mobility is provided, but since the GB mobility has a strong dependence on GB structure, e.g. misorientation angle, the concentration of impurities, precipitations, it is a rather rough estimation for GB mobility. In order to have a deep understanding of GB

motion, those parameters should be studied separately. The study of GB mobility, especially the influences of impurities, is of considerably practical importance.

This research focuses on the influences of impurity concentration on GB mobility. In particular, a correction to the existing theoretical model and the comparison between MD simulations and this corrected model and experiment results are provided. In the following the physical mechanisms of GB motion and the influences from solute drag are reviewed.

2.5.1. Grain boundary motion

GB motion could be divided into four fundamental categories:

1. Normal motion: it is also called GB migration and is the focus in this research. In this mode, the velocity of GB migration is perpendicular to the GB plane and one grain grows while the other grain shrinks.
2. Translation of grains parallel to the GB plane due to shear-coupling effect: In this process, the normal motion of GB is triggered by the shear parallel to GB plane. The shear coupling factor describes the relation between parallel velocity and normal velocity of the GB. This factor is a geometrical factor and independent of velocity (Figure 2.20 (b)).
3. GB sliding: this is a rigid-body translation of the grain on GB by sliding. No normal velocity would be coupled (Figure 2.20 (c)).
4. Grain rotation. It causes the change of the rotation in a small part of the grain so that the GB could move normally.

This figure has been moved out because of copyright issue.

Figure 2.20 (a) Initial bicrystal; (b) GB motion due to coupling; (c) GB sliding [31]

In reality, GB motion would occur in combination of the four categories, e.g., the tangential motion of a curved GB should also accompany with grain rotation, as well as normal motion due to the coupling effect. Those coupled phenomenon is of particular significance in nanocrystalline materials especially under mechanical deformation.

2.5.2. Grain Boundary Mobility

In the previous section, the thermodynamic requirement for GB stabilization was discussed, but in practice the more apparent factor that contributes to the GB stabilization is the kinetic properties of GB. For instance, the more stable GB would have a less possibility to move, which means the GB has a smaller mobility compared to the less stable one. A displacement of GB is equivalent to the shrink of one crystallite and the growth of the other one. As a result, a non-zero atomic flux from the shrinking GB to extensive GB must exist [25]. Therefore, from the view of atomistic movement, diffusion across the GB and GB movement has the same meaning, only with different reference frame. From the viewpoint based on a frame moving with GB, the movement of two grains with the same velocity is observed and one grain grows with the expense of shrinking of the other one. In the view of lab frame, the two grains are stationary while the GB moves with a constant velocity. So in this section, the GB movement is treated as the diffusion of atoms across the interface of two grains.

It is assumed that [25] each atom that moves across the GB with width $2b$ can be described by

$$v = 2b(\Gamma_+ - \Gamma_-) \tag{2.14}$$

Γ_+ and Γ_- are the jump frequency of atoms from one GB to the other. If there is no Gibbs free energy difference between the two grains, the GB would keep stationary. The driving force for the movement of GB would be the different of Gibbs free energy reads

$$P = -\frac{dG}{dV} \tag{2.15}$$

V is the unit volume of GB. If the migration free energy is G_{m},

$$v = 2b\left(v_{\mathrm{D}}e^{-\frac{G_{\mathrm{m}}}{kT}} - v_{\mathrm{D}}e^{-\frac{G_{\mathrm{m}}-PV}{kT}}\right) = 2bv_{\mathrm{D}}e^{-\frac{G_{\mathrm{m}}}{kT}}\left(1 - e^{-\frac{PV}{kT}}\right) \tag{2.16}$$

v_{D} is the Debye frequency and for all practical cases, $PV \ll kT$, so

$$v = 2bv_{\mathrm{D}}e^{-\frac{G_{\mathrm{m}}}{kT}}\left(1 - e^{-\frac{PV}{kT}}\right) \approx \frac{2bVv_{\mathrm{D}}}{kT}e^{-\frac{G_{\mathrm{m}}}{kT}} \cdot P = M \cdot P \tag{2.17}$$

M is the mobility of GB. Eq. 2.17 is the most commonly used method for us to get the mobility of GB.

2.5.3. Geometrical Factor that Influences Grain Boundary Mobility

It has been found experimentally that the temperature dependence on GB mobility obeys Arrhenius relation which could be described as [48]

$$M = A_0 \exp\left(-\frac{H}{kT}\right) \tag{2.18}$$

The pre-exponential factor A_0 and the activation enthalpy H are all influenced by the misorientation angle. This relation can be found in Figure 2.21. It shows that the pre-exponential factor A_0 and the activation enthalpy H has the same variance trend with misorientation angle. In fact, A_0 and H are related in a linear function as

$$H = \alpha \ln A_0 + \beta \tag{2.19}$$

α and β are constant and this relationship is referred to as the compensation effect (Figure 2.22) which will be discussed below.

This figure has been moved out because of copyright issue.

Figure 2.21 Activation enthalpy H and preexponential factor A_0 for <111> tilt boundaries in pure Al of different origin [48]

This figure has been moved out because of copyright issue.

Figure 2.22 Dependence of migration activation enthalpy on preexponential mobility factor for <111> $\sum 7$ tilt grain boundaries in Al [48]

Eq. 2.18 has another form

$$\ln M = \ln A_0 - \frac{H}{kT} = \frac{S}{k} - \frac{H}{kT} \tag{2.20}$$

where $S = k\ln A_0$ and H represent the activation entropy and enthalpy of GB mobility respectively. Eq. 2.20 defines a relation between activation entropy and enthalpy of GB mobility and this relation is called compensation effect. The consequence of compensation effect is that there exists a compensation temperature T_c, at which the mobility for all GBs with different misorientation angle are the same. A converse trend exists above and below this temperature T_c. Specifically, the GB with misorientation angle which has a higher mobility at $T < T_c$ would tend to lower than the mobilities with

other misorientation angle when $T > T_c$ (Figure 2.23). This relationship between entropy and enthalpy implies that the change of enthalpy, which represents energy change in time is related to structure change in space and the activated state of GB is not a random energy fluctuation in space and time [48]. Based on what has been discussed about GB phase transformation in Section 2.1.1, this phenomenon could be explained as a first order phase transformation. Let λ be the parameter denoting some intensive structural or chemical variable. If λ changes slightly from the reference state λ_0, the

$$S(\lambda) = S(\lambda_0) + \left.\frac{dS(\lambda_0)}{d\lambda}\right|_{\lambda=\lambda_0} \cdot (\lambda - \lambda_0) + \cdots$$

$$H(\lambda) = H(\lambda_0) + \left.\frac{dH(\lambda_0)}{d\lambda}\right|_{\lambda=\lambda_0} \cdot (\lambda - \lambda_0) + \cdots \quad (2.22)$$

Since $G = H - TS$ is at minimum, a linear approximation is accurate for slight change near equilibrium

$$\ln M\,(\lambda) = \frac{S(\lambda) - H(\lambda)/T_c}{k} = \frac{S(\lambda_0) - H(\lambda_0)/T_c}{k} + \frac{1}{k}\left.\frac{dG(\lambda_0)}{d\lambda}\right|_{\lambda=\lambda_0} \cdot (\lambda - \lambda_0) \quad (2.23)$$

For the first order phase transformation near equilibrium $dG(\lambda_0)/d\lambda|_{\lambda=\lambda_0} = 0$, so that

$$T_c = \frac{dH(\lambda_0)/d\lambda|_{\lambda=\lambda_0}}{dS(\lambda_0)/d\lambda|_{\lambda=\lambda_0}} = \left.\frac{dH(\lambda_0)}{dS(\lambda_0)}\right|_{\lambda=\lambda_0} \quad (2.24)$$

This results show that the new phase is a metastable phase that exists near equilibrium and the equilibrium state occurs near T_c.

This figure has been moved out because of copyright issue.

Figure 2.23 Mobility dependence of <111> tilt grain boundaries on rotation angle in pure Al at different temperatures [48].

2.5.4. Experimental Methods to Determine Grain Boundary Mobility

In experiments Eq. 2.17 is used to determine GB mobility. The major requirement for a feasible and reproducible experiment is a constant but small driving force that could satisfy Eq. 2.17, a continuous tracking of GB position, an accurate and controllable geometrical and chemical condition. Mainly two methods are used: curvature driven GB motion and stress induced GB motion.

Curvature driven GB motion requires a special geometries as presented in Figure 2.24. The driving force is the surface tension produced by the crooked GB, resulting in shrink of the grain Ⅱ. The advantage of this method is the maintenance of GB geometrical structure [53].

This figure has been moved out because of copyright issue.

Figure 2.24 Geometry of GB used for curvature-driven GB mobility test [48]

The method to measure the GB velocity is by the principal idea of X-ray Interface Continuous Tracking Device (XICTD) [53]. As shown in Figure 2.25, the bicrystal is placed in a goniometer in a way that one of the grains is in Bragg position to the X-ray and the other is not. Since the reflected X-ray on the Bragg position should be larger than that on the other grain, the reflected X-ray on GB should have the value in the middle of

those two values. If the X-ray is reflected on the surface of the material, the detector could measure the intensity of the reflected X-ray, which is used to determine the exact location of GB.

This figure has been moved out because of copyright issue.

Figure 2.25 The device used for GB mobility measurement in the principle of the XICTD [48]

Almost all experimental investigations on GB mobility have used the curvature driven method. However, in this method the measured mobility is the reduced boundary mobility $A = M \cdot \gamma$. Here γ is the GB energy and is hard to measure directly in experiment [49]. Moreover, the mobility of curvature driven GB is the averaged value of different geometrical structure GB due to the fact that the curved part of GB is composed of GBs with different inclined boundary sections. Since in the last section it has been mentioned that the GB orientation has huge influences on GB mobility, the curvature-driven method is not suitable for extracting the mobility of a specific type of GB.

Another method is based on stress-induced GB motion with the force provided by the free energy difference between adjacent grains in an external energetic field. Usually, a magnetically anisotropic crystalline solid with a planar GB was used in an external magnetic field. Due to anisotropic energy density of those two grains, the GB would move in order to lower the total energy. Since the magnetic driving force is the different magnetic energy density and the XICTD could still be used to determine the GB velocity. The advantage is that the curvature of GB is not necessary [49].

2.5.5. Effect of Impurities on Grain Boundary Mobility: The CLS Model

The effect of impurities on GB can be described by a regular solution model originally proposed by Cahn, Lücke and Stüwe (referred as CLS model) [1,10,19]. It is assumed in the CLS model that there is an interaction between impurities and GB and the GB migration is controlled by the diffusion of the impurities. As a result, the GB cannot move as fast as pure GB when it is loaded with impurities.

When there is segregation behavior in the GB, Cahn assumed that a triangle potential exists at the GB area with the minimum at the center of GB and the width b [2,19,23]

$$E(x) = \begin{cases} E^0 + \dfrac{E^0}{b}x, & -b \le x \le 0 \\ E^0 - \dfrac{E^0}{b}x, & 0 \le x \le b \\ 0, & else \end{cases} \tag{2.25}$$

E^0 is the ΔH^{seg} in Eq. 2.13. With this triangle potential, the solutes are attracted to the GB because of the lower potential energy. The chemical potential of the solutes is

$$\mu(x) = kT\ln C(x) + E(x) \tag{2.26}$$

It is important to notice that since $E(x)$ is defined in the frame that moves with GB, all conclusions arrived at in the following are based on the frame moving with GB, and all the parameters should be consistent with this frame.

The flux of atoms is assumed to be

$$-J = \frac{DC}{kT}\frac{\partial \mu(x)}{\partial x} = D\frac{\partial C(x)}{\partial x} + \frac{DC}{kT}\frac{\partial E(x)}{\partial x} \tag{2.27}$$

$J = vC(x) - vC_\infty$, C_∞ is the bulk concentration of solutes. From Fick's second law

$$\frac{\partial C(x)}{\partial t} = \frac{\partial}{\partial x}\left(D\frac{\partial C(x)}{\partial x}\right) = \frac{\partial J}{\partial x} \tag{2.28}$$

then

$$\frac{\partial C(x)}{\partial t} = D\frac{\partial^2 C(x)}{\partial x^2} + \left[\frac{\partial D}{\partial x} + \frac{D}{kT}\frac{\partial E(x)}{\partial x}\right]\frac{\partial C(x)}{\partial x} + \frac{C(x)}{kT}\left[\frac{\partial D}{\partial x}\frac{\partial E(x)}{\partial x} + D\frac{\partial^2 E(x)}{\partial x^2}\right] \tag{2.29}$$

Therefore

$$0 = D\frac{\partial^2 C(x)}{\partial x^2} + \left[\frac{\partial D}{\partial x} + \frac{D}{kT}\frac{\partial E(x)}{\partial x} + v\right]\frac{\partial C(x)}{\partial x} + \frac{C(x)}{kT}\left[\frac{\partial D}{\partial x}\frac{\partial E(x)}{\partial x} + D\frac{\partial^2 E(x)}{\partial x^2}\right] \tag{2.30}$$

Eq. 2.30 has the solution

$$C(x) = C_0 \exp\left\{-\frac{E(x)}{kT} - v\int_{x_0}^{x}\frac{d\eta}{D(\eta)}\right\} \times \int_{-\infty}^{x}\exp\left\{\frac{E(\xi)}{kT} + v\int_{x_0}^{\xi}\frac{d\eta}{D(\eta)}\right\}\frac{d\xi}{D(\xi)} \tag{2.31}$$

Here Eq. 2.31 is different from Eq. 2.13. It is important to explain here that Eq. 2.13 is derived from the thermodynamic equilibrium condition. But Eq. 2.31 is used when the GB is moved under a steady velocity v. In our study, there is no extra driving force on the GB except the impurity drag effect, so the GB is at thermodynamic equilibrium and the Eq. 2.13 is valid. What is more, in the study below the concentration of impurities in GB is independent of velocity under low-velocity limit, so Eq. 2.31 could still be used to get the GB concentration at a particular location of GB and the velocity would not appear in our derivation of mobility.

As mentioned by Cahn *et al.* [19,50], an solute will exert a force $-(dE/dx)$ on the boundary. The total force is

$$P_s = -N_V \int_{-\infty}^{+\infty} (C(x) - C_\infty) \frac{dE}{dx} dx \tag{2.32}$$

When the velocity small enough to satisfy

$$\frac{1}{v} > \int_{-b}^{b} \frac{dx}{dD(x)} \tag{2.33}$$

The concentration could be simplified to

$$C(x) = C_\infty e^{-\frac{E(x)}{kT}} \left\{ 1 + v \int_{-b}^{x} \frac{e^{-\frac{E(\xi)}{kT}} - 1}{D(\xi)} d\xi + o(v^2) \right\} \tag{2.34}$$

Substituting Eq.2.34 to Eq. 2.32

$$P_s = 4N_V C_\infty v kT \int_{-\infty}^{+\infty} \frac{\sinh^2[E(x)/2kT]}{D(x)} dx \tag{2.35}$$

Integration Eq.2.35 using the potential described in Eq. 2.25,

$$P_s = \frac{\alpha C_\infty v}{1 + \beta^2 v^2}, \alpha = \frac{2bN_V (kT)^2}{E_0} \left[\sinh\left(\frac{E_0}{kT}\right) - \frac{E_0}{kT} \right], \beta^2 = \frac{\alpha kT}{2N_V E_0^2 D} \tag{2.36}$$

When the total driving force is to be derived, the intrinsic drag $P_0(v)$, which is the drag of thermal fluctuation, should be defined. Here Cahn assumed that $P_0(v)$ is independent of composition in the practical composition range [19]. With this assumption the total driving force is

$$P\big(v, C(x)\big) = P_0(v) + P_s\big(v, C(x)\big) \tag{2.37}$$

And the relation between driving force and velocity is

$$P = \lambda v + \frac{\alpha C_\infty v}{1 + \beta^2 v^2} \tag{2.38}$$

λ is the intrinsic drag coefficient and is the reciprocal of the intrinsic mobility. When $v \ll 1/\beta$, Eq. 2.38 becomes

$$P = (\lambda + \alpha C_\infty) v \tag{2.39}$$

Based on the equation 2.24, the mobility of GB under low-velocity limit is

$$M = \frac{1}{1/M^0 + 1/M^{\mathrm{sol}}}, M^{\mathrm{sol}} = \frac{D}{2bN_V}\frac{1}{C_\infty}\frac{E_0}{(kT)^2}\left[\sinh\left(\frac{E_0}{kT}\right) - \frac{E_0}{kT}\right]^{-1} \tag{2.40}$$

Since the diffusivity D is assumed to be bulk diffusivity of solutes, it should be independent of concentration and location in the GB area under dilute solute limit. Eq. 2.40 is used in our research to extract GB mobility. However, it will be shown in Chapter 4 that Eq. 2.40 needs to be corrected by using the intrinsic GB diffusivity of the solute, instead of the bulk diffusivity assumed in the original model.

CHAPTER 3 METHODOLOGY

In this research, LAMMPS software package is used as our simulation tool. LAMMPS is the acronym for "Large-scale Atomic/Molecular Massively Parallel Simulator", which is a molecular dynamics simulation program coded developed by Sandia National Laboratories [51]. In order to understand LAMMPS package, it is crucial for us to understand what molecular dynamics simulation is and how it works.

3.1. Molecular Dynamics Simulation

Molecular Dynamics (MD) simulation is an atomistic simulation tool that can calculate and record the equilibrium parameters (e.g., energy, temperature) and transport properties (e.g., velocity, force, acceleration) of materials. All the calculations are based on the Laws of classical mechanics. Only when the translational or rotational, vibrational motion frequency ν satisfies $h\nu > kT$ and the quantum effects is evident. For a large range of materials and measurement, it is an accurate approximation to use the classical mechanics [52].

MD simulation is very similar to real experiments, in which a statistical property for a given system or predict the average behavior of a system is predicted when one or some of the system's statistical properties are known. Therefore, MD simulation follows the same steps as in experiment.

1. Prepare the sample: create a system containing a particular number of atoms with particular volume, temperature, energy as required.

2. Initialize the system: assign the initial position and velocity to all the atoms in the simulation cell.
3. Solve Newton's equations of motion for all the atoms. This step is critical and also the most time consuming.
4. Using the force obtained from step 3 to update the position and velocity of each atom.
5. Repeat step 3 and 4 until the desired length of time is used.

3.1.1. Initialization

To start the simulation, the first thing needed to do is to create atoms and assign position and velocity to each atom. The initial assignment of position is usually done by placing atoms on a cubic lattice. Then a velocity of a uniform distribution is added to each atom. Subsequently, each velocity is subtracted with the averaged velocity so that the total momentum is zero and scale the velocity to adjust the mean kinetic energy to the desired temperature. The relation between mean square velocity and temperature is

$$\langle v_\alpha^2 \rangle = \frac{3kT}{m} \tag{3.1}$$

v_α is the α component of the total velocity. And the instantaneous temperature is defined as

$$kT(t) \equiv \sum_{i=1}^{N} \frac{m v_{\alpha,i}^2(t)}{3N} \tag{3.2}$$

3.1.2. The Force Calculation and Equation of Motion

If two atoms are close enough, the interaction force between them needs to be computed. For example, the *x*-component of the force is

$$f_x(r) = -\frac{\partial U(r)}{\partial x} = -\left(\frac{x}{r}\right)\left(\frac{\partial U(r)}{\partial r}\right) \tag{3.3}$$

In MD, the potential file $U(r)$ needs to be chosen before the force calculation. In this research the EAM potential is used. EAM is the abbreviation for embedded atom model potential. In this potential, the internal energy $U(r)$ is composed of two terms

$$U(r) = \sum_i F_i\left(\sum_{j\neq i}\rho_j(R_{ij})\right) + \frac{1}{2}\sum_{ij,j\neq i}\phi_{ij}(R_{ij}) \tag{3.4}$$

F_i is the energy required to place atom *i* to the homogeneous environment with the local electron density ρ_j. $\rho_j(R_{ij})$ is the contribution to the electron charge density from atom *j* at the location where atom *i* is sited. $\phi_{ij}(R_{ij})$ is a pair-wise potential function. F_i, $\rho_j(R_{ij})$ and $\phi_{ij}(R_{ij})$ are fitted to experimental or first-principles results so that important material properties such as lattice constants, melting point, elastic modulus, etc., can be reproduced by using those potentials. This is why EAM potential is also called semi-empirical potential. EAM potential was particularly suitable to study metallic bonding, which has been used in many previous researches related to the mechanical and thermodynamic properties of metals [53].

Force calculation, e.g., the one based on Eq. 3.4, is the most time consuming part of all MD simulations. This potential implies that if only the interaction between a

particular atom and its nearest neighbor is considered, the total number of pair distance is $N(N-1)/2$ and the time needed for calculation scales as N^2.

After the force on each atom has been computed, it is now possible to integrate Newton's equations of motion to get the new position for each atom. The Taylor expression is usually used:

$$r(t+\Delta t) = r(t) + v(t)\Delta t + \frac{f_t(r)}{2m}\Delta t^2 + \frac{\Delta t^3}{3!}\dddot{r} + \mathrm{o}(\Delta t^4) \tag{3.5}$$

$$r(t-\Delta t) = r(t) - v(t)\Delta t + \frac{f_t(r)}{2m}\Delta t^2 - \frac{\Delta t^3}{3!}\dddot{r} + \mathrm{o}(\Delta t^4) \tag{3.6}$$

Summing Eq. 3.5 and Eq. 3.6,

$$r(t+\Delta t) + r(t-\Delta t) = 2r(t) + \frac{f_t(r)}{m}\Delta t^2 + \mathrm{o}(\Delta t^4)$$

$$r(t+\Delta t) \approx 2r(t) - r(t-\Delta t) + \frac{f_t(r)}{m}\Delta t^2 \tag{3.7}$$

In this method the new position has an error of the order Δt^4. The velocity can be derived from:

$$r(t+\Delta t) - r(t-\Delta t) = 2v(t) + \mathrm{o}(\Delta t^3)$$

$$v(t) = \frac{r(t+\Delta t) - r(t-\Delta t)}{2\Delta t} + \mathrm{o}(\Delta t^2) \tag{3.8}$$

It is important to mention here that it is impossible for MD simulation to predict the trajectory of each atom. All the systems studied by MD simulation are in the range where the trajectory of each atom in the $6N$ phase space (including the atom's coordinates and momenta) is very sensitive to the initial conditions. A tiny change of

initial condition could cause an exponentially increased difference in the simulation results. So it is sometimes critical to run multiple simulations with slightly different initial conditions so that the intrinsic material properties can be determined.

Besides LAMMPS, there are some other software packages that have been frequently used in this thesis research. AtomEye is the software to visualize atomistic configuration. It supports both parallel and perspective projection methods and it is very suitable for studying defects in crystalline material [54]. In addition, it has many customizable functions. In this research, it has been used to record the coordinate number of atoms and use this information for colour-encoding to reflect the defects and GB in our model so that the defects can be visible by this function. Order parameter is a reflection of the deviation of one atom from its perfect atom position and will be discussed in detail in Section 3.2. In this research, the order parameter and atom type have been selected to color-encoding the model in AtomEye. AtomEye could also render a sequence of jpeg files, which could be compressed into a movie.

3.2. Molecular Dynamics Simulation Methods on Grain Boundary Motion

Existing methods that have been developed based on MD simulations to extract GB mobility can be generally grouped to two different categories: the “driven motion method” and “fluctuation method”. The driven motion method applies a force on GB to make the GB move. The obtained velocity can be used to get GB mobility according to Eq. 2.24. Based on different origins of the driving force, the first category can be divided into three methods: curvature driven method, applied strain method, and synthetic driving

force method. The fluctuation method extracts mobility from GB thermal fluctuation and there is no need of any driving force.

3.2.1. Driven Motion Method

3.2.1.1. Curvature Driven Method

The curvature-driven GB movement is the most common technique used to determine GB mobility in experiment, but this method cannot determine the mobility for a flat GB plane without any curvature. Since the GB structure, especially the misorientation angle, could not be equivalent on the whole GB plane with a huge curvature, this method can only get averaged results of GBs of different misorientation.

There are also some simulation works by using the curvature driven method [55,56]. The same structure as in the experimental methods was used, which is shown below. The same equation used in experiment is still used here to get the reduced mobility, which is the product of mobility and GB energy.

This figure has been moved out because of copyright issue.

Figure 3.1 Schematic representation of the U-shaped half-loop [62]

The typical evolution of displacement vs. time is shown in Figure 3.2. There are three stages in this Figure: the initial stage is an “unpinning” progress, in which period of time the GB undertake some slight shape changed; after this period of time is the stead-state migration, which is used to extract the reduced mobility. The last stage occurs when the GB reaches closely to the boundary, which is set frozen to avoid the entire simulation

cell from translating or rotating. Being blocked by those frozen atoms, the GB slows down and finally stops moving. This method still cannot get the mobility directly. Moreover, due to the discreteness of the atomic structure of the GB, the length of GB would be larger than expected on the basis of continuum mechanism. As a result, a large-enough half-loop width is essential, which is very time-consuming in MD simulation.

This figure has been moved out because of copyright issue.

Figure 3.2 The time dependence of the area of the U-shaped half-loop grain A as the grain boundary migrates [62]

3.2.1.2. Applied Strain Method

This method is used by Zhang, Mendelev *et al*. [57–59] in their research to extract GB mobility. The basic idea is to use the anisotropic properties of crystalline material in space to introduce different stored elastic energy density in different grains, which can be used to drive GB motion. The elastic energy density stored in a grain is

$$F = \frac{1}{2}\sigma_{ij}\varepsilon_{ij} \tag{3.9}$$

where i and j are different coordinate axis in space. Suppose grains A B contact each other to form a GB. Let the *x*, *y*, *z* coordinates coincide with grain A and the misorientation angle is θ, the GB plane is in the *xy* plane. In Zhang's simulation cell, the surfaces with normal $\pm z$ are free, which means $\sigma_{zz} = \sigma_{xz} = \sigma_{yz} = 0$ and there is no shear stress on the GB. The stress components for grain A is:

$$\begin{aligned} \sigma_{xx} &= C_{11}\varepsilon_{xx} + C_{12}\varepsilon_{yy} + C_{12}\varepsilon_{zz} \\ \sigma_{yy} &= C_{12}\varepsilon_{xx} + C_{11}\varepsilon_{yy} + C_{12}\varepsilon_{zz} \\ \sigma_{zz} &= C_{12}\varepsilon_{xx} + C_{12}\varepsilon_{yy} + C_{11}\varepsilon_{zz} \end{aligned} \tag{3.10}$$

All shear stress and strain are zero. Let $\varepsilon_{xx} = \varepsilon_{yy} = \varepsilon$. ε_{zz} is calculated from the constraint $\sigma_{zz} = 0$. This gives the free energy of grain A

$$F_A = \frac{(C_{11} - C_{12})(C_{11} + 2C_{12})}{C_{11}} \varepsilon^2 \tag{3.11}$$

The elastic energy in grain B is found using Hooke's law,

$$F_B = \frac{(C_{11} - C_{12})(C_{11} + 2C_{12})[8(C_{11} - C_{12} + C_a) - C_a(1 - \cos(4\theta))]}{2[4C_{11}(C_{11} - C_{12} + C_a) - (C_{11} + C_{12})C_a(1 - \cos(4\theta))]C_{11}} \varepsilon^2 \tag{3.12}$$

where $C_a = 2C_{44} - C_{11} + C_{12}$ is a measure of anisotropic factor.

The driving force for GB migration is the different in the stored energy densities

$$P = F_B - F_A$$

$$= \frac{(C_{11} - C_{12})(C_{11} + 2C_{12})^2 C_a \sin^2(2\theta)}{C_{11}[4C_{11}(C_{11} - C_{12} + C_a) - (C_{11} + C_{12})C_a(1 - \cos(4\theta))]} \varepsilon^2 \tag{3.13}$$

The difference in stored energy is attributed to the misorientation angle.

This figure has been moved out because of copyright issue.

Figure 3.3 The mean grain boundary position vs. time at 1200 K and applied strain $\varepsilon = 0.02$ of pure Ni system with misorentation angle 36.8^o [59]

From the slope of mean GB position vs. time in Figure 3.3, the GB velocity was determined to be 11.25m/s, which is an uncommon high velocity for GB in crystalline material. Another disadvantage of this method is that the velocity-driving force relation is not linear even at some small strain like 0.02 [59]. Although it could be solved by reducing the applied stress, it would require considerably extra amount of computational resources and the results would be unduly influenced by thermal fluctuations.

3.2.1.3. Synthetic Driving Force Method

Janssens *et al.* [4] has put forward a new method permitting calculation of GB mobility for flat plane. They added an external energy on one grain while keeping the energy of the other grain unchanged. The method they used to distinguish between two adjacent grains is order parameter. The order parameter ξ_i for each atom *i* is defined as

$$\xi_i = \sum_j \left| \boldsymbol{r}_\mathrm{j} - \boldsymbol{r}_\mathrm{j}^\mathrm{I} \right| \tag{3.14}$$

The sum is over the *N* nearest-neighbour atoms *j* of *i*, and $\boldsymbol{r}_\mathrm{j}^\mathrm{I}$ is the nearest ideal lattice site of crystal I to $\boldsymbol{r}_\mathrm{j}$. In f.c.c. crystal *N* is 12. If the local orientation is exactly the same as perfect crystal I, the order parameter is zero. It would be positive for any deviation from perfect orientation.

Now for the situation where atom *i* in a perfect lattice *j*, the order parameter is

$$\xi_\mathrm{IJ} = \sum_\mathrm{j} \left| \boldsymbol{r}_\mathrm{j}^\mathrm{J} - \boldsymbol{r}_\mathrm{j}^\mathrm{I} \right| \tag{3.15}$$

Since Lattice I and J has different orientation, just as different grains, the order parameter in Eq. 3.15 is positive. In this way it is easy to distinguish the two grains. On the definition of order parameter an orientation-dependent potential energy is added on every atom. The artificial potential $\mu_\xi(\boldsymbol{r}_\mathrm{i})$ is

$$\mu_\xi(\boldsymbol{r}_\mathrm{i}) = \begin{cases} 0 & \xi_\mathrm{i} < \xi_\mathrm{l} \\ \dfrac{V}{2}(1 - \cos 2\omega_\mathrm{i}) \text{ with } \omega_\mathrm{i} = \dfrac{\pi}{2}\dfrac{\xi_\mathrm{i} - \xi_\mathrm{l}}{\xi_\mathrm{h} - \xi_\mathrm{l}} & \xi_\mathrm{l} < \xi_\mathrm{i} < \xi_\mathrm{h} \\ V & \xi_\mathrm{i} < \xi_\mathrm{h} \end{cases} \tag{3.16}$$

$\xi_l = f\xi_{IJ}$, $\xi_h = (1-f)\xi_{IJ}$. The value f is chosen to subtract the error due to thermal fluctuation. The effect of this potential is that atoms of from one grain would now have a potential energy larger than the potential energy of the other grain. Consequently, GB movement would occur to shrink one grain with higher energy while extending the low-energy grain. The extra force is given as:

$$\mathbf{F}(\boldsymbol{r}_i) = -\frac{\partial \mu_\xi}{\partial \boldsymbol{r}_i} = -\frac{\pi V}{2(\xi_h - \xi_l)}\left\{\left(\sum_j \frac{\boldsymbol{\delta}_{ij}}{|\boldsymbol{\delta}_{ij}|}\right)\sin 2\omega_i + \sum_j\left[-\frac{\boldsymbol{\delta}_{ji}}{|\boldsymbol{\delta}_{ji}|}\sin 2\omega_i\right]\right\} \quad (3.17)$$

This equation only valid for $\xi_l < \xi_i, \xi_j < \xi_h$ and $\boldsymbol{\delta}_{ij} = \boldsymbol{r}_i + \mathbf{I}_{ij} - \boldsymbol{r}_j$, $\mathbf{I}_{ij} = \boldsymbol{r}_j^I - \boldsymbol{r}_i$. For ξ_i, ξ_j outside the given limit, $\mathbf{F}(\boldsymbol{r}_i)$ is zero. Eq. 3.11 requires that $\mathbf{F}(\boldsymbol{r}_i)$ would be nonzero only for those atoms having a nonzero partial derivative of μ_ξ to $\boldsymbol{r}_i$. Those atoms can only exist at the transition area from one grain to the other, which is exactly the GB area. This flat GB would move similar with the GB movement under volumetric driving force such as magnetic field. One example is shown in Figure 3.4. This Figure is the plot of average positions of two GB with the same structure of [111] symmetric mixed-type GB in nanocrystalline Al. The GB velocity is constant through the entire simulation, and from the slope the velocity of GB and the mobility could be determined based on Eq. 2.24. However, one drawback of this method is that the velocity is too high to be realistic. In this simulation, the velocity for GB is 0.79Å ps^{-1}, which is 79ms^{-1}. In the case with high concentration of impurities, it will be impossible for the solutes to catch up with GB under this velocity by diffusion mechanism. What is worse, the linear relation between velocity and driving force describe by Eq. 2.24 is only valid under small driving force limit; it is quite possible that the mobility might develop a driving force dependence

under such a high driving force. Therefore, the so-called fluctuation method will be needed to extract the mobility of GB with the presence of impurity atoms.

This figure has been moved out because of copyright issue.

Figure 3.4 Example of the GB motion of nanocrystalline Al at 800 K and V=0.025 eV[4]

3.2.2. Fluctuation method

3.2.2.1. Interface Random Walk Method

The driven force method has been successfully used to extracte the GB mobility with no curvature but has the limitation of unrealistic high driving force. In order to extend the driving force to more realistic value, another problem would rise on the time and space limit of MD simulation. For MD simulation, the simulation time would be around tens of nanoseconds. Thus, in order to get a statistical meaningful data, the GB need to be forced to move an appropriate length within a short time interval. Consequently, the driving force must be large again.

There is a novel method proposed by Trautt *et al*. [9] to be able to extract GB mobility under zero driving force limit based on purely the thermal fluctuation of the GB. It is based on the fact that the GB would fluctuate around its equilibrium position at any given temperature in a way similar to the typical random walk behavior. This is why this method is normally referred as interface random walk (IRWalk) method. It has been shown that after a long period of time, the average derivation of GB from its equilibrium position is zero while the mean square displacement of GB will increase with time among a large number of independent simulations of identical geometry and temperature but different initializations.

To confirm this behavior, Trautt *et al*. [9]has performed MD simulations in crystalline Al at 750K. Both LJ and EAM potentials were used. Figure 3.5 shows the model structure and the distribution of average interface displacement of GB. The distribution is clearly Gaussian at each of the four time intervals and the symmetrical distribution of the displacement reveals that there is no influence between the two GBs. The Gaussian nature of the distribution proves that the GB movement is indeed random walk behavior and a "diffusion coefficient" *D* similar to the diffusivity in atomistic diffusion is defined

$$D = \frac{\langle \overline{h^2} \rangle}{t} \tag{3.18}$$

h is the displacement of GB at the time interval t.

In the continuum limit, the normal interface velocity v of GB is associated with the capillary driving force $\kappa_\gamma$and the intrinsic thermal fluctuation η

$$v = M\left(\kappa_\gamma + \eta\right) \tag{3.19}$$

The capillary force is the product of the interface mean curvature and its stiffness, $\Gamma\kappa$. If the GB displacement in z direction as shown in Figure 3.5 is represented as h, κ is expressed as the sum of second partial derivative of the height of GB with respect to x and y direction when $\partial h/\partial x \ll 1, \partial h/\partial y \ll 1$. Intrinsic thermal fluctuation η is an uncorrelated function of space and time. So Eq. 3.19 is expressed as

$$v = \frac{\partial h}{\partial t} = M\left(\Gamma\left(\frac{\partial^2 h}{\partial x^2} + \frac{\partial^2 h}{\partial y^2}\right) + \eta(x, y, t)\right) \tag{3.20}$$

Integrating both sides of Eq. 3.20 in space and time and applying the relation between diffusivity and mean square displacement in random walk, $\langle\overline{h^2}\rangle = Dt$

$$D = \frac{2MkT}{A} \tag{3.21}$$

A is the interface area within the simulation cell. This is the method used in our simulation to get the diffusivity and mobility of GB. Neither the driving force nor artificial GB curvature is needed. Moreover, it is possible for us to study the segregation effect on GB motion with a much smaller simulation cell.

Figure 3.5 Left: Schematic of the fully periodic computational cell. Right: Distribution of the average interface position with respect to the initial position in the EAM-Al simulations [9]

3.2.2.2. Adapted Interface Random Walk Method

Although IRWalk method [9] can be used to extract the GB mobility at zero driving force limit, a large number of independent simulations are usually needed so that the random walk behavior of the GB can be properly accessed. In order to save simulation time and improve the accuracy of the result, a new data processing method is adpated.

For example, if there are 20 independent simulations of 10 *ns* duration, and the GB positions are recorded every 5 ps, in order to extract the GB mobility *M*, the displacement $d(i)$ after $5i$ *ps* can be calculated based on the GB position $p(i)$ by $d(i) = p_j\big((l+1)i\big) - p_j(li), \Big(l = 0,1,\dots,[\frac{2000}{\mathrm{i}}], j = 1,2\dots 20, i = 1,2\dots 2000\Big)$. With

this adaptation, an equivalent of 20× $[\frac{2000}{\mathrm{i}}]$ independent data points can be obtained for GB displacement $d(i)$ during $t = 5i$. Accordingly, the variance of GB displacement $\langle \bar{d}^2(i) \rangle$during time $t = 5i$ can be calculated as:

$$\langle \bar{d}^2(i) \rangle = \frac{1}{20\left\lfloor \frac{2000}{i} \right\rfloor} \sum_{j=1}^{20} \sum_{l=0}^{\left\lfloor \frac{2000}{i} \right\rfloor} \left(p_j\big((l+1)i\big) - p_j(li) \right)^2 \tag{3.22}$$

CHAPTER 4 SIMULATION MODEL AND PROCEDURE

An inclined $\sum 5$ GB in three types of Al-based alloys was simulated by MD using LAMMPS [33] with embedded-atom method potentials including Al-Ni [34], Al-Pb [35], and Al-Ti [36] with time step of 5 fs. Various concentrations of impurity atoms (Ni, Pb, or Ti) were introduced into the model by randomly replacing Al atoms at the GB region prior to the simulations. The initial simulation cell was set to be 5.69 nm × 5.69 nm × 10.48nm in *x*, *y* and *z* directions (Figure 4.1), respectively, accommodating 20608 atoms. As shown in Figure 4.1(a), the dopant (Ni) atoms were initially placed at the GB region randomly. The Al atoms in Figure 4.1(b) were removed to show dopant atoms only. Periodic boundary conditions were applied along the *x* and *y* directions while the two surfaces perpendicular to the z-axis were free. Isothermal-isobaric ensemble (NPT) was used for the first 100 ps to relax the model and canonical ensemble (NVT) was used afterwards for all simulations. For each alloy system of a specific concentration, 20 simulations (different random velocity initialization) up to 10 ns were performed. Atomic configurations of each alloy system were visualized by AtomEye [60]. The GB position can be determined by using an order parameter which depends on the local lattice orientation [61,62]. The system temperature T is equal to 750K, 775K, 800K, 825K, and 850K, respectively. In this research, only the GB properties in high temperature range were studied so that significant GB fluctuation can be observed in these alloys.

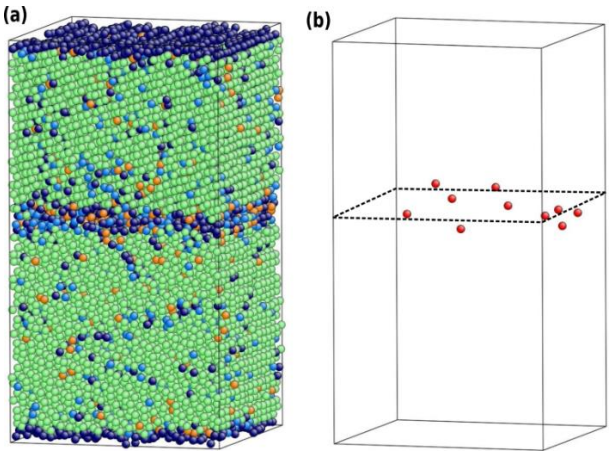

Figure 4.1 The initial atomistic configurations of the simulation cell in Al-Ni. In (a) the atom color corresponds to local lattice orientation [63,64] and in (b) only the impurity (Ni) atoms are shown.

CHAPTER 5 RESULTS AND DISCUSSION

5.1. Impurity Segregation and Thermal Fluctuation of the Grain Boundary

As shown in Figure 5.1(a), the dopant atoms were initially placed at the GB region. Here the atom color on the left corresponds to an order parameter that depends on the local lattice orientation [4,61,62]; the Al atoms on the right were removed to show dopant atoms only. Depending on the alloy system, the dopant atoms behaved dramatically different as the GB fluctuated and moved away from its original position. Representative results were shown in Figure 5.1(b)-(d) for systems containing 10 Ni, Pb, and Ti dopant atoms respectively with the black and red dashed lines marking the initial and current average GB positions. It is found that Ni atoms moved along with the GB which indicated strong segregation (Figure 5.1(b)), Pb atoms aggregated and formed a precipitation which also moved along with the GB (Figure 5.1(c)), whereas Ti atoms were left behind the migrating GB and almost stayed at their original positions. It is worth mentioning that in all these systems the GB has moved a substantial distance away from its initial position.

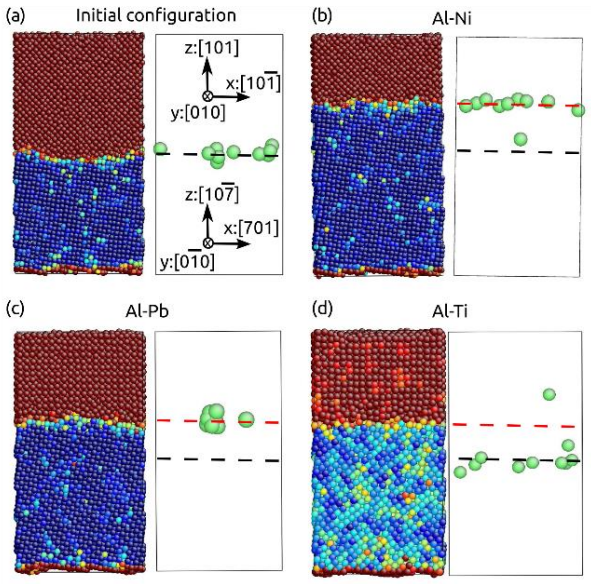

Figure 5.1 (a) The initial and current atomistic configurations of the simulation cell during the GB thermal fluctuation in (b) Al-Ni, (c) Al-Pb, and Al-Ti. On the left the atom color corresponds to an order parameter depending on the local lattice orientation and on the right only dopant atoms are shown. The black and red dashed lines mark the initial and current GB positions, respectively.

While GB segregation and precipitation has been commonly observed in experiments [18] and studied by both analytical modeling [18] and Monte Carlo simulations [65,66], it is encouraging to observe clear solute segregation and precipitation by direct MD simulations. In order to confirm that the GB segregation and precipitation shown in Figure 5.1 was not transitional, the evolution of the average GB position was compared with the center-of-mass (COM) of the dopant atoms of different solute concentrations in both Al-Ni and Al-Pb alloy systems; one example is shown in Figure 5.2(a)-(b) for Al-Ni with 2 and 40 Ni atoms respectively. It can be seen that in both cases, the evolution of the COM of Ni atoms and the average GB position almost overlapped each other for up to 10 ns. Moreover, the evolution of GB displacement up to 10 ns among 20 independent simulations in Al-Ni alloy system with 2 and 40 Ni atoms was shown in Figure 5.2(c) and 5.2(d). It is found that solute segregation would not affect

the random walk behavior of the GB during thermal fluctuation and the higher the dopant concentration, the smaller the variance of GB fluctuation.

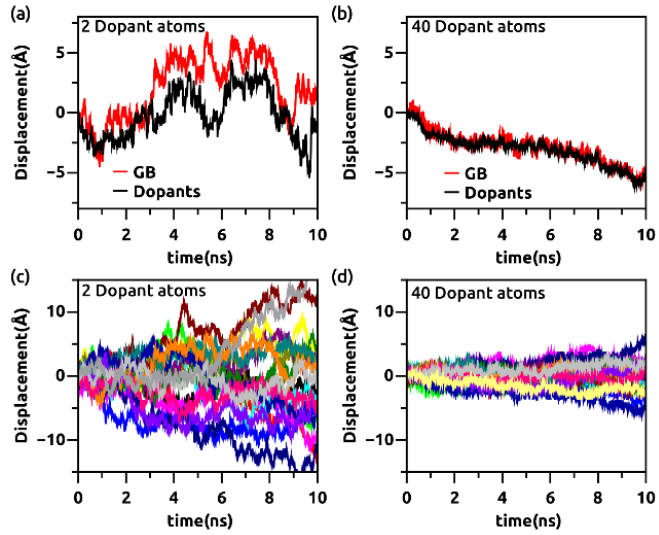

Figure 5.2 Evolution of the displacement of GB and the center-of-mass of dopant atoms in Al-Ni system with (a) 2 and (b) 41 Ni atoms. Evolution of the average GB displacement in Al-Ni containing (c) 2 and (d) 41 Ni atoms based on 20 independent simulations.

5.2. Extraction of Grain Boundary Mobility from IRWalk Method

Since the thermal fluctuation of the GBs with impurities still showed the random walk behavior (Figure 5.2), it is now possible to extract the GB mobility from the adapted IRWalk method that has been explained in Section 3.2.2.2. The representative results were shown in Figure 5.3. In Figure 5.3 (a) and Figure 5.3(b), the evolution of the variance of GB displacement with time was plotted for different dopant concentrations in Al-Ni and Al-Pb, which consistently showed a linear trend as predicted by Eq. 3.18. The GB mobility at various dopant concentrations in both Al-Ni and Al-Pb was then extracted according to Eq. 3.18 and plotted in Figure 5.1(c); it is clearly shown that the GB mobility decreased as the number of dopant atoms increased in both systems. This trend

is in excellent agreement with past experimental studies[25], analytical modeling[2,18,23,66], and indirect MD simulations [67]. For example, Mendelev and Srolovitz [23,66] have predicted that the GB mobility was inversely proportional to the bulk concentration for the case of attraction of impurities to the boundary based on the CLS model. Mendelev and Srolovitz[67] have also used MD simulations to parameterize the CLS model in Al-Fe system and confirmed that the segregated Fe impurities would slow down the GB migration.

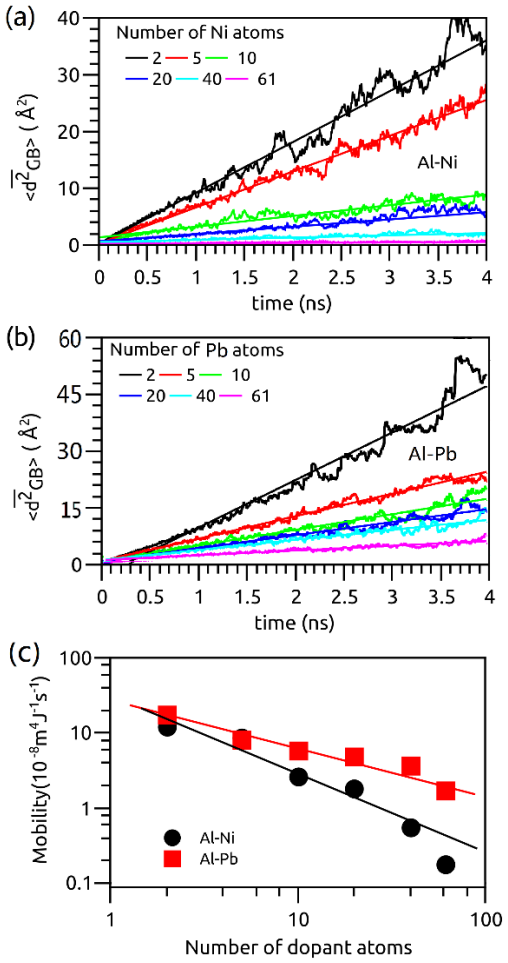

Figure 5.3 (a) The evolution of the variance of average GB displacement in Al-Ni. (b) The evolution of the variance of average GB displacement in Al-Pb. (c) GB mobility as a function of the number of dopant atoms in both Al-Ni and Al-Pb.

In order to validate that the IRWalk method can indeed be extended to extract physical mobility of GBs containing impurities, the mobility of the same Al-Ni GB with 10 Ni atoms in the GB area was also extracted by the artificial driving force method [4,62,68] based on Eq. 2.17, $V = MP$, where V is the GB velocity due to an applied driving force P, and M is the GB mobility. Here a relatively small driving force of $P = 0.98\ MPa$ was applied to ensure that the linear relationship between GB velocity and the applied driving force is not significantly deviated[62] and that the dopant atoms can catch up with the moving GB. As shown in Figure 5.4(a), under this driving force all the solutes could move along with GB, which means the segregation behavior was independent of the simulation methods. The GB displacement from 20 independent simulations for the same GB but with different initial conditions was plotted in Figure 5.4(b), which shows similar random walk behavior as in Figure 5.2. However, the average displacement among the 20 simulations due to the applied driving force showed an linear increase with time, as plotted in Figure 5.4(c), the slope of which is the GB velocity ($V = -0.026\ m/s$). The mobility for Al-Ni system with 10 Ni atoms in GB based on this method was thus calculated to be $2.70 \times 10^{-8} m^4 J^{-1} s^{-1}$, which is consistent with $2.61 \times 10^{-8} m^4 J^{-1} s^{-1}$ that extracted from the same GB based on the IRWalk method. This is strong indication that the existing MD methods that were developed based on pure systems can be applied to extract physical mobilities of GB with impurity segregation.

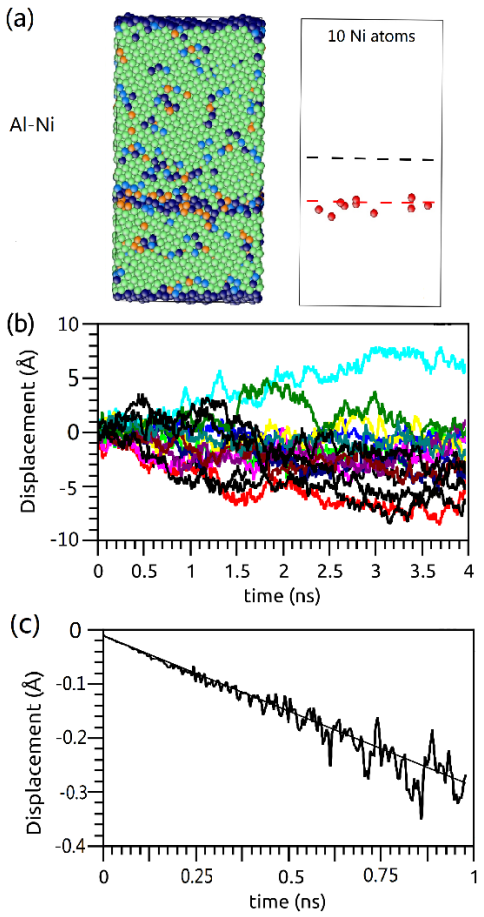

Figure 5.4 (a) The initial and current atomistic configurations of the simulation cell during the GB thermal fluctuation in Al-Ni. The black and red dashed lines mark the initial and current GB positions, respectively. Evolution of the (b) individual and (c) average GB displacement in Al-Ni containing 10 Ni atoms with driving force of 0.98MPa among 20 independent simulations.

5.3. Grain Boundary Diffusion of Segregated Impurities

Since it has been proposed in the CLS theory that the mobility of a migrating impure boundary is controlled by the impurity diffusion [10,19,23], the diffusional behavior of the segregated dopant atoms in the Al-Ni system were investigated systematically. Specifically, the dopant diffusivity was extracted by using the Einstein relation $D^{x}_{dopant} = < x^2 > / 2t$ for diffusion along x direction (parallel to the GB) and $D^{z}_{Dopant} = < z^2 > / 2t$ for diffusion along the z direction (perpendicular to the GB) [69]. At

each dopant concentration, the evolution of the mean square displacement (MSD) of the dopants and the corresponding dopant diffusivity was analysed in two different ways: the results in Figures 5.5(a), 5.5(b) and 5.5(c) were based on the absolute movements of individual dopant atoms and the results in Figures 5.6(a), 5.6(b) and 5.6(c) were based on movements of individual dopant atoms relative to their COM. Specifically, Figure 5.5(a) and 5.6(a) showed the evolution of absolute and relative MSD of Ni atoms along z direction (MSD^z) in Al-Ni system containing 5 Ni atoms at the GB. While a general linear trend was found between the MSD^z and t as predicted by the Einstein relation in both Figures 5.5(a) and 5.6(a), it was surprising to see the significant variance among the 20 independent simulations. Although such variance was similar to that in Figures 5.2(c)-(d), it was not caused by the thermal fluctuation of the GB because in Figure 5.6(a) the variance was reduced but not completely cancelled out by eliminating the overall drift of the Ni atoms along with the GB plane. In the past, it was not uncommon to extract the dopant diffusivity in MD [69] by applying the Einstein relation based on only one single simulation, which could be considerably inaccurate by sampling only a small portion of the possible behaviors of the dopant atoms as indicated by Figures 5.5(a) and 5.6(a).

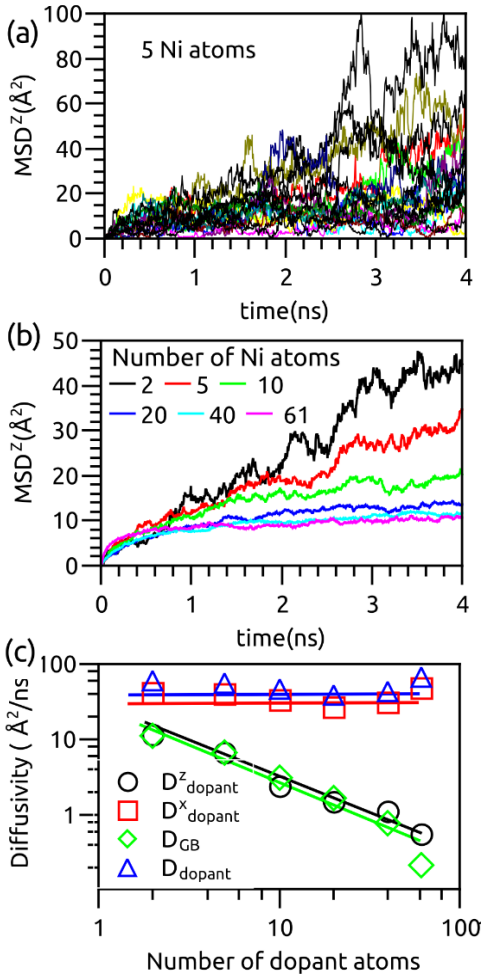

Figure 5.5 (a) The evolution of the absolute MSD of impurities perpendicular to the GB plane in Al-Ni containing 5 Ni atoms. (b) The average of absolute MSD of dopant atoms as a function of the number of dopant atoms among 20 independent simulations. (c) The absolute diffusivity of the dopant atoms as a function of the number of dopant atoms. In (c), the superscripts *x* and *z* denote the directions parallel and perpendicular to the GB, subscript "dopant" denotes absolute dopant diffusivity. Solid lines are added as guide to the eye in (c). D_{GB} is the parameter used in Eq. 3.18.

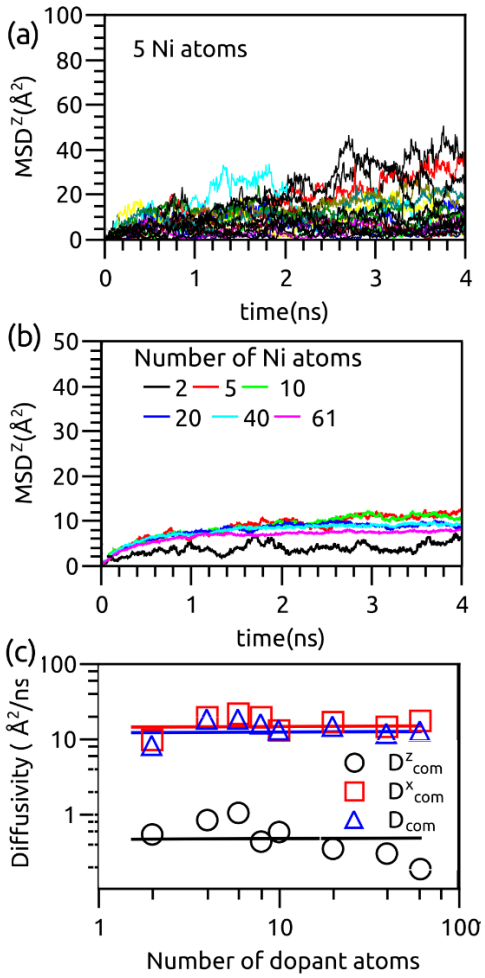

Figure 5.6 (a) The evolution of the MSD of impurities relative to the COM of the impurity atoms perpendicular to the GB in Al-Ni containing 5 Ni atoms. (b) The average of MSD relative to the COM of dopant atoms as a function of the number of dopant atoms among 20 independent simulations. (c) The diffusivity of the dopant atoms relative to the COM as a function of the number of dopant atoms. In (c), the superscripts *x* and *z* denote the directions parallel and perpendicular to the GB, subscript "dopant" denotes absolute dopant diffusivity and "COM" denotes dopant diffusivity relative to their COM. Solid lines are added as guide to the eye in (c).

Furthermore, it was found that the absolute dopant diffusivity perpendicular to the GB (D^z_{Dopant}) has a strong dependence on the solute concentration; as shown in Figure 5.5(c), the slope of MSD^z *vs. t* decreased dramatically as the number of Ni atoms increased. Based on the Einstein relation, D^z_{Dopant} was extracted and plotted in Figure

5.5(c), which decreased as the dopant concentration increased. It is interesting to find that the "diffusion" coefficient D_{GB} used to extract the GB mobility M as defined in Eq. 3.18 was almost the same as D^z_{Dopant} (Figure 5.5(c)). A strong correlation between the GB mobility M and the diffusivity of dopant atoms perpendicular to the GB D^z_{Dopant} can thus be established. In contrast, the diffusivity parallel to the GB (D^x_{Dopant}) remained relatively unchanged at all solute concentrations (Figure 5.5(c)). Since the dopant diffusion parallel to the GB was significantly larger than that perpendicular to the GB ($D^x_{Dopant} >> D^z_{Dopant}$), the overall GB diffusivity of Ni atoms (D_{Dopant}) also remained relatively unchanged at different solute concentrations (Figure 5.5(c)). However, by eliminating the overall drift of Ni atoms along with the GB and extracting the diffusivity of Ni atoms relative to their COM (Figures 5.6(b) and 5.6(c)), the strong dependence of dopant diffusivity perpendicular to the GB on concentration no longer existed. For example, D^z_{com}, D^x_{com} and D_{com}, which denote the diffusivity of Ni atoms relative to their COM in the direction perpendicular to the GB, parallel to the GB, and the overall GB diffusivity, all showed weak or none dependence on the concentration (Figure 5.6(c)).

5.4. The Modification of CLS Model

With the GB mobility and solute diffusivity extracted from direct MD simulations, it is now possible to quantitatively validate the CLS model. As suggested by Mendelev *et al.* [6,19,23], the mobility of an impure GB based on the CLS model can be expressed as

$$M = \frac{1}{1/M^0 + 1/M^{\mathrm{sol}}}, M^{\mathrm{sol}} = \frac{D}{2bN_V}\frac{1}{C_\infty}\frac{E_0}{(kT)^2}\left[\sinh\left(\frac{E_0}{kT}\right) - \frac{E_0}{kT}\right]^{-1} \qquad (2.40)$$

where M^0 is the GB mobility in pure system, N_V is the number of dopant atoms per unit volume of the GB, b is the GB thickness, E_0 is the heat of segregation for impurity, C_∞ is the bulk dopant concentration, and D is the bulk diffusivity of the dopant. When there was no impurity, the GB in our model moved considerably faster than those with dopants. For some initial conditions the GB could even move out of the model within 1 *ns*. Therefore, it is reasonable to assume that M^0 is so large that the GB mobility M would be dominated by M^{sol} according to Eq. 2.40.

C_∞ is the bulk dopant concentration which correlates with the dopant concentration segregated at the GB C_0 [6,23] according to:

$$X_\beta^{\mathrm{GB}} = X_\beta^{\mathrm{M}} \exp\left(\frac{\Delta H^{\mathrm{seg}}}{RT}\right) \tag{2.13}$$

where ΔH^{seg}, X_β^{GB} and X_β^{M} are E_0, C_0 and C_∞ respectively. Here a similar method was used as in Ref. [6] to determine the segregation energy E_0. First the model containing 10 dopant atoms in the GB was fully relaxed at 850K and zero pressure under NPT, then the temperature was reduced to 0 K in a stepwise fashion with the step of 50 K and 0.1 ns relaxation for each step under NPT. The same process was then performed on the same model, but the 10 dopant atoms were randomly placed in the bulk instead of in the GB. The difference of energy for those two models at T = 0 K divided by the number of impurity atoms is the segregation energyE_0 [6]. For Ni segregation in Al for the inclined Σ5 GB considered in this study, this energy was found to be -0.446 eV/atom. Although zero bulk concentration with all dopant atoms segregated to the GB in simulations has been assumed in this study, Eq. 2.13 can still be used to estimate C_∞ that may lead to the same C_0 studied in this research.

According to the original CLS model, D in Eq. 2.40 is the bulk diffusivity of dopant atoms. It was found that the bulk diffusion of Ni in Al obeyed the Arrhenius equation [70]:

$$D = Ae^{-\frac{Q}{kT}} \tag{5.1}$$

A is a frequency factor and Q is the activation energy. For Al-Ni system, $A = 4.4 \times 10^{-4} m^2 s^{-1}$, $Q = -145.8 kJ\text{mol}^{-1}$ [70]. Since the applicable temperature range for this value [70] is 742-924K, it is appropriate for us to use this equation in estimating the bulk diffusion coefficient of Ni in Al system, which is $4.79374 \times 10^{-13} m^2 s^{-1}$. It is very important to mention that the bulk diffusivity from the potential used in this study, which can be determined only through Monte Carlo simulations, would not be the same as the experimental value. However, since the bulk and GB diffusivity normally differ by several orders of magnitude, the experimental value ($4.79 \times 10^{-13} m^2 s^{-1}$) is considered to be reasonable as compared to the GB diffusivity predicted by the interatomic potential as shown in Figure 6 (e.g., $D^z_{COM} \approx 5 \times 10^{-12} m^2 s^{-1}$, $D_{COM} \approx 1.5 \times 10^{-10} m^2 s^{-1}$).

Another factor needed to be determined is the GB thickness. Since the solutes introduced were initially located in GB, it is reasonable to predict that the thickness of GB based on the strong segregation behavior of solutes in GB shown in Figure 5.2. Figure 5.7 (a) plotted the solutes distribution in GB in z direction for 0 and 3.5 ns respectively. A clear trend of diffusion across the total GB area is shown and after 3.5 ns the majority of the solutes are within the range of 1 nm. To test whether the distribution of solutes at 3.5 ns is in their equilibrium state or not, all the solute positions were fitted

to a cumulative distribution function. This method has been used by Deng and Schuh [61,62] and has the following function

$$F(x) = \frac{1}{2}\left[1 + \mathrm{erf}\left(\frac{x-\mu}{\sigma\sqrt{2}}\right)\right] \tag{5.2}$$

$F(x)$ is the possibility for solute position to fall within the interval $(-\infty, x]$. erf is the error function. μ and σ are the averaged value and variance for all the solute positions. The error function in Eq. 5.2 is a result of integration of Gaussian distribution into a cumulative form and could also be used to check whether all the data points fit into Gaussian distribution or not. The results at t = 0, 2.5, 5.4 ns are plotted respectively in Figure 5.7 (b). All the solute positions at the three different times fit into error function pretty well. This is another evidence of random thermal fluctuation of solutes as shown in Figure 5.6. Although the difference between t = 0 and t = 2.5 ns is obvious, there is little variance between the distribution of 2.5 ns and 5.4 ns, which is an indication of thermal equilibrium state. Therefore, the variance of position shown in Figure 5.7 (a) will not change significantly with time and 1 nm was regarded as the GB thickness.

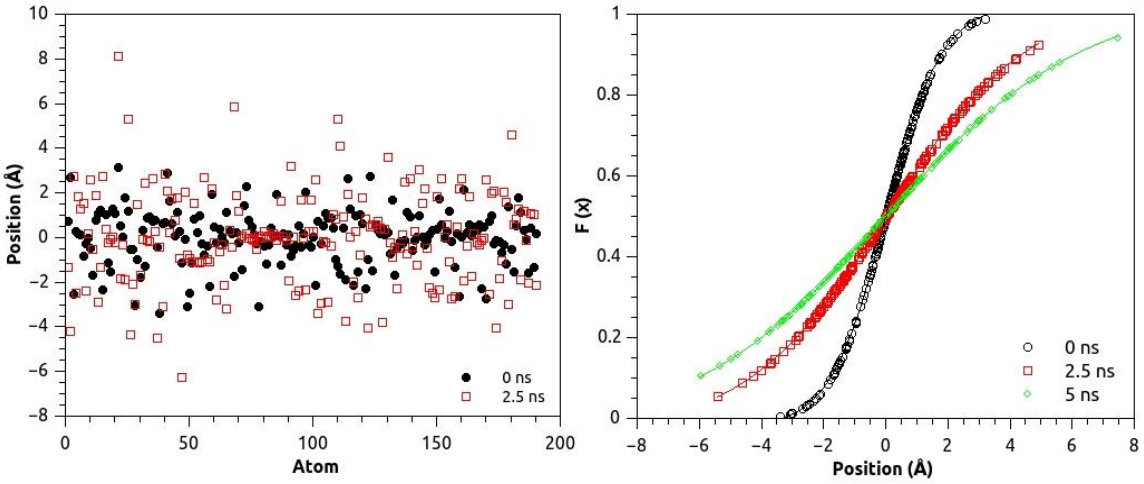

Figure 5.7 (a) solutes distribution in GB. The black markers are initial solutes distribution at 0 ns. The red markers are distribution after 3.5 ns. (b) The cumulative frequency for the position of solutes in GB.

With the proper parameters determined, the results by fitting Eq. 2.40 with the bulk diffusivity of Ni in Al system ($4.79 \times 10^{-13} m^2 s^{-1}$[70]) were shown in Figure 5.8 with green diamond (denoted as CLS1). It can be seen that the fitted results were significantly smaller than those from the direct MD simulation (solid black circle). Nevertheless, the slopes of both trend lines were more or less the same. Since Figure 5.5(c) suggested that the GB mobility mostly correlated to the solute diffusion perpendicular to the GB plane, the discrepancy between our simulation results and the fitting from Eq. 2.40 may stem from the use of bulk diffusivity of Ni in Al for D. Therefore, Eq. 2.40 was fitted again by replacing D with D^z_{Dopant} while other parameters remained the same; the results were shown in Figure 5.8 with blue triangle (denoted as CLS2). However, although the newly fitted results became closer to the simulation results in magnitude, the trend lines now differed significantly in slope. Therefore, another constant but propitiate value of D is necessary.

In the original CLS model and that developed by Mendelev and Srolovitz [23], *D* refers to the bulk impurity diffusivity. For example, Mendelev and Srolovitz have used MD simulations to investigate the GB segregation and solute drag effects in Al-Fe system by parameterizing the CLS model [6], in which the bulk diffusivity of Fe in Al was used for the parameter *D*. However, since the impurities mainly locate at GB region in strongly segregated system, the impurity diffusion during the GB migration should be also limited to the GB plane. It is thus expected that the solute drag effects should be only relevant to GB impurity diffusion, or more specifically, the diffusion of impurity atoms in the direction perpendicular to the GB plane. It is also worth mentioning that Equations 2.40 were derived in the coordinate system that translates with the migrating GB [19,23]. Accordingly, it is important that the impurity diffusivity should also be determined in the same coordinate system.

Furthermore, since the intrinsic GB mobility M^0 is significantly larger than M^{sol} at the high temperatures used in this study (750K – 850K), the overall GB mobility *M* described in Equation 2.40 can be approximated by $M \approx M^{\mathrm{sol}}$. For example, at 850 K the intrinsic GB mobility M^0 was found to be so large that the GB itself would quickly disappear during the thermal fluctuation.

By applying the aforementioned adaptation to *D* and the simplification with $M \approx M^{imp}$, Eq. 2.40 can be rewritten in the following form as:

$$M^{\mathrm{sol}} = \frac{D^{z}_{\mathrm{Dopant}}}{2bN_V}\frac{1}{C_\infty}\frac{E_0}{(kT)^2}\left[\sinh\left(\frac{E_0}{kT}\right) - \frac{E_0}{kT}\right]^{-1} \tag{2.40}$$

By combining Eq. 2.40 and Eq. 5.1 and assuming Arrhenius relation for the GB diffusivity of Ni in Al along the *z* direction (the direction perpendicular to the GB)

$D^{z}_{Dopant} = D_{0}{}^{z}_{Dopant} \exp(-\frac{Q_D}{kT})$, Eq. 2.40 can also be expressed in the form of GB concentration C_0 instead of bulk concentration C_∞:

$$M^{\mathrm{sol}} = \frac{D^{z}_{\mathrm{Dopant}}}{2bN_V} \frac{\exp\left(-\frac{Q_{\mathrm{D}} + E_0}{kT}\right)}{C_0} \frac{E_0}{(kT)^2} \left[\sinh\left(\frac{E_0}{kT}\right) - \frac{E_0}{kT}\right]^{-1} \tag{5.3}$$

where Q_D is the activation energy for GB diffusion of Ni in Al along the *z* direction. In this study, the following parameters have been determined to be: b = 1 nm, $N_V = 62.2\ nm^{-3}$ and $E_0 = -0.446eV$ as in [71].

According to John Cahn [23], an expression for the impurity flux is given as

$$-J = \frac{DC}{kT}\frac{\partial \mu(x)}{\partial x} = D\frac{\partial C(x)}{\partial x} + \frac{DC}{kT}\frac{\partial E(x)}{\partial x} \tag{2.27}$$

Since the COM of dopant atoms always moved along with the GB in Al-Ni as shown in Figure 5.4(c) and Figure 5.4(d), the diffusivity of Ni in the frame of the moving GB would be perfectly approximated by the relative diffusion coefficient D^{z}_{com} as shown in Figure 5.6(c). Also, based on John Cahn's model [23], b is not the total GB thickness but half of it. Further corrections to the CLS model can thus be made by replacing D^{z}_{Dopant} in CLS2 by D^{z}_{com}. Here the average of D^{z}_{com} at different concentrations shown in Figure 5.6(c) was used to fit Eq. 2.20. The newly fitted results based on D^{z}_{com} were denoted as CLS3 in Figure 5.8 with orange squares, which perfectly matched the MD simulation results in both the slope and magnitude.

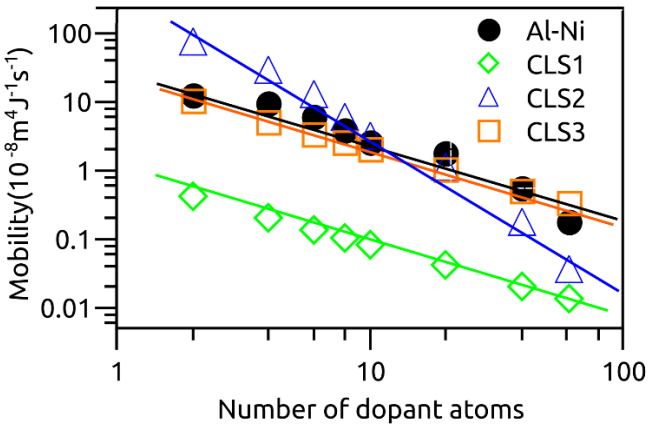

Figure 5.8 Theoretical predictions based on CLS model by using bulk diffusivity D (CLS1), D^{z}_{Dopant} (CLS2) and D^{z}_{com} (CLS3) in Al-Ni system. Solid lines are added as guide to the eye.

5.5. Temperature Effects on Grain Boundary Mobility

Since it has been found that Ni atoms would strongly segregate to the GB in Al and move along with the GB during the thermal fluctuation (Figure 5.2), based on the above discussion, the mean square displacement (MSD) of impurity atoms along z direction ($< z^2 >$) in the reference of the moving GB can be obtained by tracking the movement of individual Ni atoms relative to their COM. This corrected CLS model fitted with the simulation results quite well, and in this section the influences of temperature on GB mobility is studied.

The representative results of impurity GB diffusivity were shown in Figure 5.9. In Figure 5.9(a) and Figure 5.9(b), the time evolution of the MSD of Ni atoms relative to their COM was plotted at different dopant concentrations at 800K. Here the GB concentration was calculated in such a way that the total number of GB atoms was assumed to be constant (2000 atoms). It can be seen from Figure 5.9(a) that even at 800K, the MSD evolution has weak or no dependence on the impurity concentration. Therefore,

all the MSD curves obtained from various concentrations at each temperature were averaged and plotted them in Figure 5.9(b). The impurity diffusivity D^{z}_{Dopant} was thus extracted according to the Einstein relation and plotted in Figure 5.9(c), which showed a clear Arrhenius trend. The activation energy was determined to be Q_D = 1.40 ± 0.07 eV within the temperature range studied in this work.

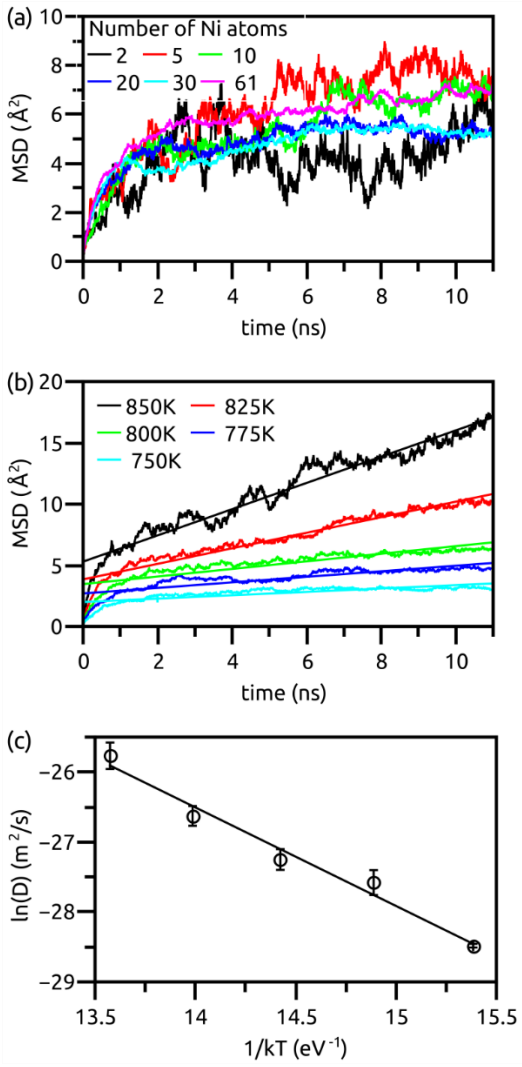

Figure 5.9 (a) The evolution of the MSD of Ni atoms relative to their COM in the direction perpendicular to the GB plane at six different GB concentrations. (b) The average MSD of Ni atoms relative to their COM at different temperatures. (c) Arrhenius plot of the intrinsic GB diffusivity of impurity atoms in the direction perpendicular to the GB plane.

With the diffusivity D^{z}_{Dopant} determined from Figure 5.9, the GB mobility with the presence of different concentration of Ni can be calculated based on the adapted CLS model (Eq. 5.3). For comparison purposes, the GB mobility calculated from Eq. 5.3 and that obtained from MD simulations with IRWalk method were plotted in Figure 5.10(a) and 5.10(b) in both linear and log scales, respectively. It can be seen from Figure 5.10 that the MD simulation results agreed with predictions from the adapted CLS model fairly well, although at relatively low temperatures and high impurity concentration (e.g., T = 750K and C_0 > 0.005) severe discrepancy can be sensed. Such discrepancy, however, might be mainly due to the limitation of IRWalk method because the GB fluctuations under these conditions would become too subtle to be tracked properly. Nevertheless, the general trend that the GB mobility (*M*) should be inversely proportional to the impurity concentration ($C_0 \; or \; C_\infty$) at constant temperature, as predicted by Equations 5.3, was well captured by the MD simulations. The overall good agreement between MD simulations and the theoretical prediction thus provides strong support for the validity of the CLS theory on modeling solute drag effects on GB motion.

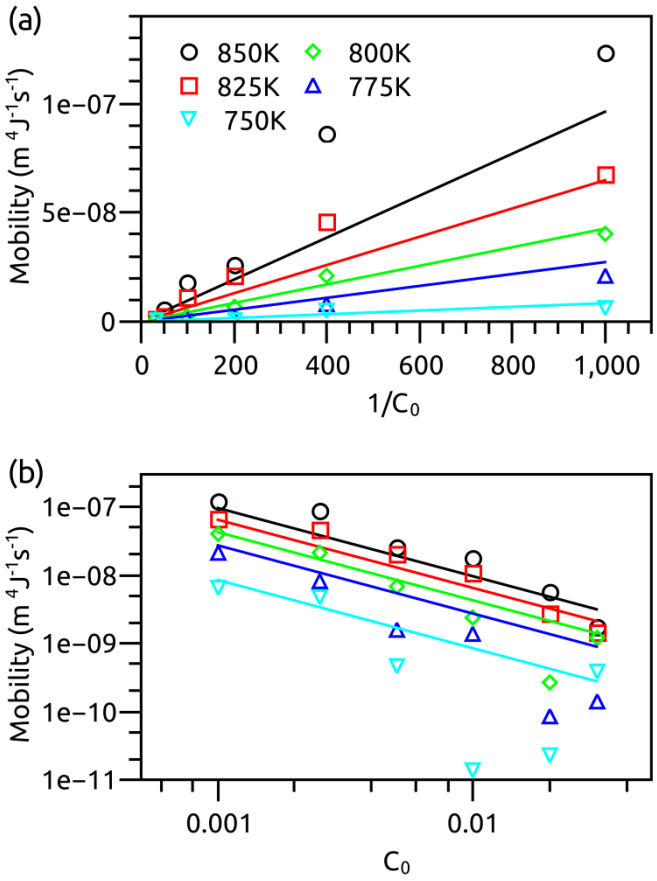

Figure 5.10 GB mobility as a function of impurity GB concentration (C_0) in (a) the linear and (b) log scale, respectively.

5.6. Activation Energy for Grain Boundary Motion

In order to further prove the validity of the adapted CLS model, the activation energy for GB motion were extracted in the Al-Ni system based on results from both MD simulations and calculations according to Eq. 5.2 (Figure 5.11). It can be seen from Figure 5.11 (a) that the activation energy (E_m), which is proportional to the slope of each curve, is consistent between MD simulations and that predicted from the adapted CLS model. Here only the data points collected at relatively low concentrations (C_0 = 0.1% ~ 1%) have been included; due to the difficulty of accurately measuring the GB mobility

with the IRWalk method at high impurity concentrations, large uncertainty would be expected for the determination of activation energy at C_0 > 1%.

The activation energy extracted from the four low concentration simulations (C_0 = 0.1% ~ 1%) and the theoretical predictions based on the adapted CLS model were plotted in Figure 5.11 (b). In order to be consistent with results from past experiments and atomistic simulations, which were also included in Figure 5.11 (b), the activation energy was plotted as a function of the bulk concentration C_∞. Specifically, the experimental activation energies were determined from both an inclined $\sum 5$ <100> GB (the same misorientation in our model, open circles) and a non-special <100> tilt GB (the filled triangles), and the previous theoretical predictions were from Mendelev et al. [6] based on a non-symmetric $\sum 5$ GB in Al-Fe system by parameterizing the original CLS model (the black solid line). For MD simulation results in this study, the bulk concentration can be estimated from Eq.5.1. Since the temperature range considered in this study was relatively narrow (750K ~ 850K), the bulk concentrations determined at different temperatures were close to each other especially on the log scale. For example, for GB concentration of C_0 = 0.1%, the corresponding bulk concentrations were calculated to be $C_\infty = 2.2536 \times 10^{-6}$ and $C_\infty = 1 \times 10^{-6}$ at T = 850 K and 750 K, respectively. Therefore, the bulk concentration at T = 800 K was plotted in Figure 5.11(a).

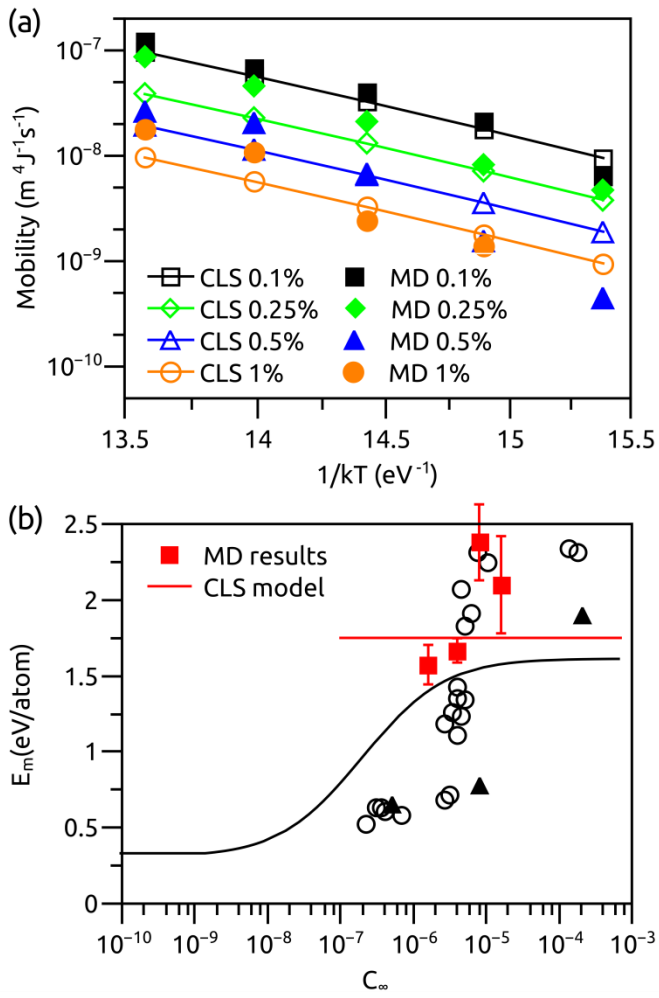

Figure 5.11 (a) Arrhenius plot of GB mobility extracted from MD simulations and adapted CLS model at different impurity GB concentrations (C_0 = 0.1% ~ 1%). (b) The dependence of the activation energy on bulk concentration (C_∞) for $\sum 5$ ⟨100⟩ tilt GB in Al-Ni alloy system. Bulk solid line was obtained from Mendelev et al. [6]. The squares and triangles represent the experimental data for the mobilities of $\sum 5$ ⟨100⟩ and a non-special ⟨100⟩ tilt grain boundaries, respectively [11]. The filled red squares and the red solid line are results from current MD simulation and the adapted CLS model, respectively.

It is extremely interesting to find out that the activation energies extracted from current MD simulations agreed very well with past experimental studies. This is strong indication that the IRWalk method used in this study can be used to extract accurate mobility of GB that contains segregated impurities. On the other hand, however, the

theoretical results from the adapted CLS model showed constant a constant activation energy (the red solid line, E_m = 1.73 eV) for all impurity concentrations, which is similar to the predictions by Mendelev et al. from the original CLS model (the black solid line) at the high concentration limit. It needs to be mentioned that at relatively low impurity concentrations, the GB mobility should become close to that from pure systems ($M^{sol} \approx M^0$). According to Mendelev et al. [6], the activation energy should gradually decrease to that for the pure system as the impurity concentration decreases.

While Figure 5.11 (b) seems to suggest that the adapted CLS model is incapable of predicting the upper limit of the activation energy for GB motion with high concentration of impurities, the mismatch between MD simulation results and the theoretical predictions might be partially due to the inaccurate measurement of the GB mobility from the IRWalk method. Alternative methods or adaptations to the IRWalk method are needed to improve the accuracy of the GB mobility measurement, which warrants future study.

On the other hand, although the MD results were found to be in good agreement with past experimental results, a direct comparison between them should be made with caution. For example, the experimental results shown in Figure 5.11(b) were based on reduced GB mobility A which was obtained according to [6]

$$A = M(\gamma + \gamma'') \tag{5.4}$$

γ is the boundary free energy and $\gamma''$is its second derivative with respect to boundary inclination. Another difficulty is that simulations and experiments consider physically different systems. Simulations only focus on one kind of solute and ignore all the other

impurities or dislocations, while truly pure materials do not exist. Some solutes might have the inverse effect as the Ni solute in GB, while the GB might undertake complexion transformation, or even turn into liquid near melting temperature [26]. Also, when a GB enters a high concentration area of solutes, it might bulge out or break away at those sites, thus decreasing the solute drag effects on GB mobility[8]. Finally, the heat of segregation of Ni to GB also depends on GB structure and the potential used, which might be quite different from the experimental condition.

CHAPTER 6 SUMMARY

In summary, an adaptation has been made of the CLS theory model describing GB motion by replacing the impurity bulk diffusivity by the impurity diffusion in the direction perpendicular to the GB motion. The adapted CLS model was further validated by direct MD simulations with the IRWalk method. In particular, four major conclusions can be made based on the results from this research:

1. It is possible to observe segregation behavior both in Al-Ni and Al-Pb $\sum 5$ inclined GB directly by molecular dynamics simulation, which is assumed to be impossible in previous study.
2. In Al-Ni and Al-Pb system, the segregation behavior of dopants in $\sum 5$ inclined GB do not influence the random walk behavior, which enables the extension of the interface random walk method to extract the GB mobility with the presence of segregate impurities.
3. $\sum 5$ inclined GB mobility in Al-Ni alloy is significantly influenced by the segregated impurities and decreases as the impurity concentration increases.
4. In the CLS theory model describing GB mobility, the intrinsic GB diffusivity of impurities in the direction perpendicular to the GB plane, instead of the bulk diffusivity assumed in many previous studies, should be used to accurately describe the GB motion with the presence of impurities.

5. MD simulation results of Al-Ni $\sum 5$ inclined GB motion with segregated Ni atoms are consistent with that adapted CLS model and the experimental results at the temperature range 750K to 850K.

In particular, two journal publications and one conference presentation have been produced based on these results:

Publications:

- *Adapted solute drag model for grain boundary motion with segregated impurities.* Hao Sun and Chuang Deng, under review
- *Direct quantification of solute effects on grain boundary motion by atomistic simulations.* Hao Sun and Chuang Deng, under review

Talks:

- *Influences of Solute Segregation on Grain Boundary.* Materials Science & Technology 2013 Conference and Exhibition, Montreal, Quebec, Canada

It should be mentioned however, the discrepancy on activation energy between MD simulation results and theoretical predictions suggest that more accurate determination of GB mobility or further adaptation of the CLS model is needed before the deep correlation between GB motion and the presence of impurity can be established. Future studies are warranted regarding realistic segregation conditions and temperature effects by Monte Carlo simulation. In addition, at low temperature the MD simulation tends to become inaccurate and it is hard for us to extract an accurate mobility from the interface random walk behavior, so alternative simulation method will be needed to study GB motion at low temperature for future works.

REFERENCE

[1] Lücke K., and Detert K., 1957, "A quantitative theory of grain-boundary motion and recrystallization in metals in the presence of impurities," Acta Metallurgica, **5**(11), pp. 628–637.

[2] Mendelev M. I., and Srolovitz D. J., 2001, "A regular solution model for impurity drag on a migrating grain boundary," Acta Materialia, **49**(4), pp. 589–597.

[3] Deng C., and Schuh C. A., 2011, "Atomistic Simulation of Slow Grain Boundary Motion," Phys. Rev. Lett., **106**(4), p. 045503.

[4] Janssens K. G. F., Olmsted D., Holm E. A., Foiles S. M., Plimpton S. J., and Derlet P. M., 2006, "Computing the mobility of grain boundaries," Nature Materials, **5**(2), pp. 124–127.

[5] Deng C., and Schuh C. A., 2011, "Diffusive-to-ballistic transition in grain boundary motion studied by atomistic simulations," Physical Review B, **84**(21), p. 214102.

[6] Mendelev M. I., Srolovitz D. J., Ackland G. J., and Han S., 2011, "Effect of Fe Segregation on the Migration of a Non-Symmetric Σ5 Tilt Grain Boundary in Al," Journal of Materials Research, **20**(01), pp. 208–218.

[7] Zhang H., Du D., and Srolovitz D. J., 2008, "Effects of boundary inclination and boundary type on shear-driven grain boundary migration," Philosophical Magazine, **88**(2), pp. 243–256.

[8] Rollett A. D., Gottstein G., Shvindlerman L. S., and Molodov D. A., 2004, "Grain boundary mobility – a brief review," Zeitschrift für Metallkunde, **95**(4), pp. 226–229.

[9] Trautt Z. T., Upmanyu M., and Karma A., 2006, "Interface Mobility from Interface Random Walk," Science, **314**(5799), pp. 632–635.

[10] Lücke K., and Stüwe H. P., 1971, "On the theory of impurity controlled grain boundary motion," Acta metallurgica, **19**(10), pp. 1087–1099.

[11] Gottstein G., and Shvindlerman L. S., 1999, Grain boundary migration in metals: thermodynamics, kinetics, applications, CRC press.

[12] Klement U., Erb U., El-Sherik A. M., and Aust K. T., 1995, "Thermal stability of nanocrystalline Ni," Materials Science and Engineering: A, **203**(1-2), pp. 177–186.

[13] Millett P. C., Selvam R. P., and Saxena A., 2007, "Stabilizing nanocrystalline materials with dopants," Acta Materialia, **55**(7), pp. 2329–2336.

[14] Detor A. J., and Schuh C. A., 2011, "Microstructural evolution during the heat treatment of nanocrystalline alloys," Journal of Materials Research, **22**(11), pp. 3233–3248.

[15] Millett P. C., Selvam R. P., and Saxena A., 2006, "Molecular dynamics simulations of grain size stabilization in nanocrystalline materials by addition of dopants," Acta Materialia, **54**(2), pp. 297–303.

[16] Trelewicz J. R., and Schuh C. A., 2009, "Grain boundary segregation and thermodynamically stable binary nanocrystalline alloys," Phys. Rev. B, **79**(9), p. 094112.

[17] Chookajorn T., Murdoch H. A., and Schuh C. A., 2012, "Design of Stable Nanocrystalline Alloys," Science, **337**(6097), pp. 951–954.

[18] Trelewicz J., and Schuh C., 2009, "Grain boundary segregation and thermodynamically stable binary nanocrystalline alloys," Physical Review B, **79**(9).

[19] Cahn J. W., 1962, "The impurity-drag effect in grain boundary motion," Acta Metallurgica, **10**(9), pp. 789–798.
[20] Olmsted D. L., Holm E. A., and Foiles S. M., 2009, "Survey of computed grain boundary properties in face-centered cubic metals—II: Grain boundary mobility," Acta Materialia, **57**(13), pp. 3704–3713.
[21] Zhang H., Mendelev M. I., and Srolovitz D. J., 2004, "Computer simulation of the elastically driven migration of a flat grain boundary," Acta Materialia, **52**(9), pp. 2569–2576.
[22] Suzuki A., and Mishin Y., 2003, "Atomistic Modeling of Point Defects and Diffusion in Copper Grain Boundaries," INTERFACE SCIENCE, (11), pp. 131–148.
[23] Mendelev M. I., and Srolovitz D. J., 2002, "Impurity effects on grain boundary migration," Modelling and Simulation in Materials Science and Engineering, **10**(6), pp. R79–R109.
[24] Callister W. D., 2001, Fundamentals of materials science and engineering: an interactive etext, Wiley, New York.
[25] Gottstein G., and Shvindlerman L. S., 2010, Grain Boundary Migration in Metals, CRC Press, Taylor & Francis Group, Boca Raton.
[26] Cantwella P. R., Tangb M., Dillonc S. J., Luod J., Rohrere G. S. and Harmera M. P., 2014, "Grain boundary complexions," Acta Materialia, **62**, pp. 1–48.
[27] Lejček P., 2010, Grain boundary segregation in metals, Springer-Verlag, Berlin.
[28] "Grain boundary" [Online]. Available: http://en.wikipedia.org/wiki/Grain_boundary. [Accessed: 13-Mar-2014].
[29] 2014, "Bubble raft movies (videos) and pictures" [Online]. Available: http://homepages.cae.wisc.edu/~stone/bubble%20raft%20movies.htm#pictures.
[30] Uberuaga B. P., Bai X.-M., Dholabhai P. P., Moore N., and Duffy D. M., 2013, "Point defect–grain boundary interactions in MgO: an atomistic study," Journal of Physics: Condensed Matter, **25**(35), p. 355001.
[31] Cahn J. W., Mishin Y., and Suzuki A., 2006, "Coupling grain boundary motion to shear deformation," Acta Materialia, **54**(19), pp. 4953–4975.
[32] Helmut F., "7.1.2 The Coincidence Site Lattice" [Online]. Available: http://www.tf.uni-kiel.de/matwis/amat/def_en/kap_7/backbone/r7_1_2.html. [Accessed: 16-Mar-2014].
[33] Plimpton S., 1995, "Fast Parallel Algorithms for Short-Range Molecular Dynamics," Journal of Computational Physics, **117**(1), pp. 1–19.
[34] Purja P. G. P., and Mishin Y., 2009, "Development of an interatomic potential for the Ni-Al system," Philosophical Magazine, **89**(34-36), pp. 3245–3267.
[35] Landa A., Wynblatt P., Siegel D. J., Adams J. B., Mryasov O. N., and Liu X.-Y., 2000, "Development of glue-type potentials for the Al–Pb system: phase diagram calculation," Acta Materialia, **48**(8), pp. 1753–1761.
[36] Zope R. R., and Mishin Y., 2003, "Interatomic potentials for atomistic simulations of the Ti-Al system," Physical Review B, **68**(2), p. 024102.
[37] Yoshizawa Y., Oguma S., and Yamauchi K., 1988, "New Fe-based soft magnetic alloys composed of ultrafine grain structure," Journal of Applied Physics, **64**(10), p. 6044.

[38] Gleiter H., 2000, “Nanostructured materials: basic concepts and microstructure,” Acta Materialia, **48**(1), pp. 1–29.
[39] Goddard W. A., 2012, Handbook of nanoscience, engineering, and technology, CRC Press, Boca Raton, FL.
[40] Schuh C. A., Nieh T. G., and Iwasaki H., 2003, “The effect of solid solution W additions on the mechanical properties of nanocrystalline Ni,” Acta Materialia, **51**(2), pp. 431–443.
[41] Tetelman A. S., and McEvily A. J., 1967, Fracture of structural materials, Wiley, New York.
[42] Rupert T. J., and Schuh C. A., 2010, “Sliding wear of nanocrystalline Ni–W: Structural evolution and the apparent breakdown of Archard scaling,” Acta Materialia, **58**(12), pp. 4137–4148.
[43] Detor A., and Schuh C., 2007, “Grain boundary segregation, chemical ordering and stability of nanocrystalline alloys: Atomistic computer simulations in the Ni–W system,” Acta Materialia, **55**(12), pp. 4221–4232.
[44] Millett P. C., Selvam R. P., Bansal S., and Saxena A., 2005, “Atomistic simulation of grain boundary energetics – Effects of dopants,” Acta Materialia, **53**(13), pp. 3671–3678.
[45] Herbig M., Raabe D., Li Y. J., Choi P., Zaefferer S., and Goto S., 2014, “Atomic-Scale Quantification of Grain Boundary Segregation in Nanocrystalline Material,” Physical Review Letters, **112**(12).
[46] Wolf D., and Yip S., eds., 1992, Materials interfaces: atomic-level structure and properties, Chapman & Hall, London ; New York.
[47] Tang F., Gianola D. S., Moody M. P., Hemker K. J., and Cairney J. M., 2012, “Observations of grain boundary impurities in nanocrystalline Al and their influence on microstructural stability and mechanical behaviour,” Acta Materialia, **60**(3), pp. 1038–1047.
[48] Dmitri A. M., 1998, “Grain Boundary Migration in Metals: Recent Developments,” INTERFACE SCIENCE, **6**(1-2), pp. 7–22.
[49] Günster C., Molodov D. A., and Gottstein G., 2013, “Migration of grain boundaries in Zn,” Acta Materialia, **61**(7), pp. 2363–2375.
[50] Balluffi R. W., and Cahn J. W., 1981, “Mechanism for diffusion induced grain boundary migration,” Acta Metallurgica, **29**(3), pp. 493–500.
[51] “LAMMPS Molecular Dynamics Simulator” [Online]. Available: http://lammps.sandia.gov/. [Accessed: 25-Mar-2014].
[52] Frenkel D., 2002, Understanding molecular simulation: from algorithms to applications, Academic Press, San Diego.
[53] Kutzler F., and Painter G., 1987, “Energies of atoms with nonspherical charge densities calculated with nonlocal density-functional theory,” Physical Review Letters, **59**(12), pp. 1285–1288.
[54] Li J., 2003, “AtomEye: an efficient atomistic configuration viewer,” Modelling Simul. Mater. Sci. Eng., (11), pp. 173–177.
[55] Zhang H., Upmanyu M., and Srolovitz D. J., 2005, “Curvature driven grain boundary migration in aluminum: molecular dynamics simulations,” Acta Materialia, **53**(1), pp. 79–86.

[56] Moneesh U., Smith, R. W. and David S. J., 1998, "Atomistic Simulation of Curvature Driven Grain Boundary Migration," INTERFACE SCIENCE, **6**, pp. 41–58.
[57] Upmanyu M., Smith R. W., and Srolovitz D. J. 2005, "Atomic mechanisms of grain boundary diffusion: Low versus high temperatures," Journal of Materials Science, **40**(12), pp. 3155–3161.
[58] Zhang H., Srolovitz D. J., Douglas J. F., and Warren J. A., 2007, "Atomic motion during the migration of general [001] tilt grain boundaries in Ni," Acta Materialia, **55**(13), pp. 4527–4533.
[59] Zhang H., Mendelev M. I., and Srolovitz D. J., 2004, "Computer simulation of the elastically driven migration of a flat grain boundary," Acta Materialia, **52**(9), pp. 2569–2576.
[60] Li J., 2003, "AtomEye: an efficient atomistic configuration viewer," Modelling and Simulation in Materials Science and Engineering, **11**(2), p. 173.
[61] Deng C., and Schuh C. A., 2011, "Atomistic Simulation of Slow Grain Boundary Motion," Physical Review Letters, **106**(4).
[62] Deng C., and Schuh C. A., 2011, "Diffusive-to-ballistic transition in grain boundary motion studied by atomistic simulations," Physical Review B, **84**(21).
[63] Sun H., and Deng C., 2014, "Direct quantification of solute effects on grain boundary motion by atomistic simulations," Unpublished.
[64] Li J., 2003, "AtomEye: an efficient atomistic configuration viewer," Modelling and Simulation in Materials Science and Engineering, **11**(2), p. 173.
[65] Xie X., and Mishin Y., 2002, "Monte Carlo simulation of grain boundary segregation and decohesion in NiAl," Acta Materialia, **50**(17), pp. 4303–4313.
[66] Mendelev M. I., and Srolovitz D. J., 2001, "Kink model for extended defect migration in the presence of diffusing impurities: theory and simulation," Acta Materialia, **49**(14), pp. 2843–2852.
[67] Mendelev M. I., Srolovitz D. J., Ackland G. J., and Han S., 2011, "Effect of Fe Segregation on the Migration of a Non-Symmetric Σ5 Tilt Grain Boundary in Al," Journal of Materials Research, **20**(01), pp. 208–218.
[68] Mendelev M. I., Deng C., Schuh C. A., and Srolovitz D. J., 2013, "Comparison of molecular dynamics simulation methods for the study of grain boundary migration," Modelling Simul. Mater. Sci. Eng., **21**(4), p. 045017.
[69] Frolov T., Divinski S. V., Asta M., and Mishin Y., 2013, "Effect of Interface Phase Transformations on Diffusion and Segregation in High-Angle Grain Boundaries," Physical Review Letters, **110**(25).
[70] 1998, Smithells metals reference book, Butterworth-Heinemann, Oxford ; Boston.
[71] Sun H., and Deng C., "Direct quantification of solute effects on grain boundary motion by atomistic simulations," under review.